# Protruding Fiber Configurations using DRS in Bone Awls

## Potential low-resource guidance technology for pedicle screw placement

by

Justin Douglas Heintz

Student Number

5198151

| | |
|---|---|
| Supervisors: | Jenny Dankelman |
| | Merle Losch |
| External: | Paul van Breedveld |
| Defended on: | Summer, 2023 |
| Faculty: | 3mE, Delft |

TU Delft

# Preface

Before introducing the topic of my graduation project, I want to reflect over my time in Delft and the express my gratitude to the very people that supported me throughout the entire process. I started this project with very little knowledge on the topic, but I enjoyed the challenge this presented. Due to the pandemic all but one of my courses were taught online. Having weekly in-person meetings with my incredibly supportive supervisor Merle and getting to use engineering machinery on campus was an great learning experience. Thank you to David Jager from DEMO for helping me manufacture my final probe and sharing your enthusiasm for how the relevant machines work.

I am also very grateful to my fellow students in the MISIT Lab and BITE department. The feedback sessions and workshops all helped me throughout the thesis process and added a much needed in-person interactions after the pandemic. Furthermore, I also want to thank my graduation committee, Jenny Dankelman and Paul van Breedveld for taking the time to evaluate my work. friends who supported me throughout the project.

This work would also not have been possible without the unwavering support of my family and friends. Thank you to my parents and brothers for supporting me not only during my studies, but everything else I hope to achieve as well. Your love means the world to me. Thank you to Ines, Eda, Sam, Elke and Ana for all the coffee and lunch (soup) breaks we shared on campus while working on our graduation projects. I really could not have asked for more supportive and loving friends.

Lastly, I want to dedicate this thesis to the person who motivated me to study engineering in a medical context in the first place, my sister Charlyn. Charliemaus, dieses Paper widme ich dir und ich freue mich ab jetzt mehr Zeit mit dir verbringen zu können.

*Justin Douglas Heintz*
*Delft, October 2023*

# Summary

In recent decades, spinal fixation surgery has become a routine surgery. The procedure stiffens the spine using a combination of pedicle screws and rods and eliminate any relative motion between adjacent vertebrae. The accurate placement of the pedicle screws is crucial as inaccuracies can compromise the integrity of the fixation, as well as result in damage to the surrounding tissues including the spinal column which runs through the vertebrae. State of the art guidance techniques, such as 3D printed, patient-specific guide plates help surgeons avoid misalignments. However these techniques are expensive, resource intensive and therefore inaccessible to a large percentage of the global population, highlighting the need for a more accessible alternative guidance technology. Diffuse Reflectance Spectroscopy (DRS) is a simple form of optical spectroscopy and could act a low-cost alternative to provide guidance to surgeons during the placement of the pilot holes for pedicle screws. This study proposes integrating two optical fibers into a bone awl and to use DRS as a guidance aid by warning surgeons if the tip of the awl is about to breach into an adjacent tissue.

To understand if DRS can be used for this application, the effect of the needle-shaped tip of the bone awl on the ability of the optical probe to provide the necessary guidance is explored. The light-emitting fiber is placed along the awl's edge, while the light-collecting fiber is placed in the center of the needle's tip for light-collection. This means the light-collecting fiber is protruding ahead of the light-emitting fiber and the sharper the needle, the greater this protrusion. Using Monte Carlo simulations in MATLAB and phantom experiments as the angle between the two fibers increases from 0° (blunt tip, no protrusion) to 60° in increments of 10°. The performance of the probe is assessed at each angle by determining the maximum detection depth, as well as the strength of the signal received at the light collecting fiber.

The Monte Carlo simulations yielded satisfactory detection depths (> 1mm) at all fiber configurations tested, but a significant drop in the signal strength if the needle sharpness exceeds 30°. To validate this, phantom experiments were performed using a custom designed and manufactured optical probe. The experiments suggest that the simulations were underestimating the signal strength and the sharpest angle at which the probe can provide guidance to surgeons is at 40°. At this angle, the detection depth is greater than 1mm and the signal strength was still satisfactory. These findings warrant further exploring how DRS can be integrated into a bone awl. This study primarily acts as a proof of concept and further research is required to improve the tissue identification of DRS.

# Contents

# Nomenclature

## Abbreviations

| Abbreviation | Definition |
|---|---|
| DRS | Diffuse Reflectance Spectroscopy |
| SDS | Source-to-Detector Separation |
| AF | Auto-flourescence |
| RBC | Red Blood Cell |
| LC | Light Collector |
| LE | Light Emitter |

# 1 Introduction

Owing to demographic and lifestyle changes in recent decades, spinal fusion surgery has become one of the most common surgical procedures [16, 36]. The surgery can be required due to multiple conditions including, but not limited to disease, disorder or trauma to the spine resulting in an abnormal range of motion between adjacent vertebrae. However, despite the procedure being considered routine, mistakes still occur and result in much worse patient outcomes. This includes the improper placement of the pedicle screws [3]. The correct placement of these screws is crucial for ensuring the integrity of the entire fixation, as well as minimizing postoperative pain and recovery time for patients.

To enhance the safety and efficacy of pedicle screw placement, researchers at Delft University of Technology are working on integrating optical fibers into a bone awl [21, 32, 33]. This would enable real-time feedback about the position of the tip of the bone awl during the procedure. This approach aims to provide surgeons with information about which tissue the tip of the awl is currently in and the proximity of any surrounding tissues. This helps to mitigate the risk of complications and optimize patient outcomes.

This chapter aims to provide further background information about spinal fixation surgery and introduce the key concepts concerning limited guidance options available to surgeons and how Diffuse Reflectance Spectroscopy (DRS) may provide a low-resource alternative for surgeons particularly in lower income countries.

## 1.1. Background Information

### 1.1.1. Spine Anatomy

The spine, also known as the vertebral column or backbone, is vital for providing support, flexibility, and protection to the body. It comprises of 33 stacked vertebrae, inter-vertebral discs, the spinal cord, surrounding muscles and ligaments. In addition to its structural support, the spine plays a crucial role in safeguarding the spinal cord and the nerves that extend along its length. It forms a protective canal, with inter-vertebral discs acting as cushions between the vertebrae, reducing pressure and preventing direct contact that could harm the nerves.

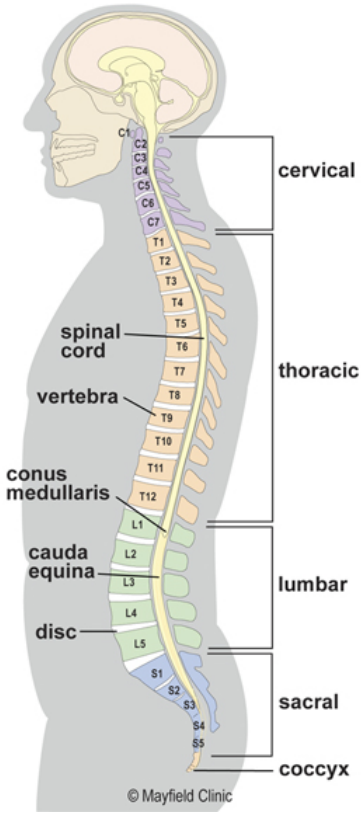


**(a)** The five regions of the spinal column (Figure adapted from [13]).

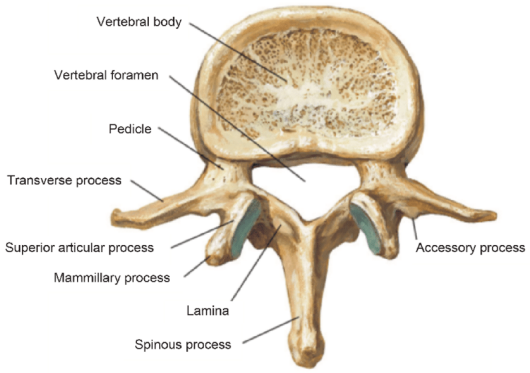


**(b)** Superior View of an L2 (Lumbar) vertebrae. The body consists of cancellous bone tissue. Pedicle screws penetrate the pedicle and enter the vertebral body which consists of cancellous bone tissue (Figure adapted from [4]).

**Figure 1.1:** Visual representation of the anatomical features of the Spinal Column

The spine is divided into five main sections: cervical, thoracic, lumbar, sacral, and coccygeal as can be seen in Figure 1.1a. The cervical spine, located in the neck, consists of seven vertebrae. The thoracic spine, found in the upper and middle back, is composed of twelve vertebrae. The lumbar spine, situated in the lower back, comprises five large vertebrae. The sacral spine consists of fused vertebrae that form the back of the pelvis, while the coccygeal region includes the tailbone. Spinal fusion surgery is typically performed on the cervical, thoracic, or lumbar sections. Each individual vertebra within the spine has its own unique anatomy. A typical vertebra consists of a rounded vertebral body located at the front, providing weight-bearing support. From the vertebral body, a bony arch extends posteriorly, forming the vertebral foramen. This arch includes the pedicles, which project backward and connect to the laminae, enclosing the spinal canal which houses the spinal chord. A visual breakdown of a vertebrae is shown in Figure 1.1b [4].

The stability of the spine is supported by a complex network of muscles, including the paraspinal muscles. These deep muscles run along both sides of the spine and play a crucial role in maintaining proper posture, enabling controlled movement, and protecting the spine from excessive stress or strain.

The bones of the spine are made up of different types of bone tissue. The outer portion of the vertebrae consists of cortical bone, which provides strength and protection. The center of the vertebrae contains spongy cancellous bone, which is lighter and

more flexible. This spongy bone contains marrow and offers structural support while allowing for shock absorption and distribution of loads [8].

### 1.1.2. Spinal fusion surgeries

Spinal fusion, also referred to as spinal fixation surgery has become one of the most commonly performed procedures [36]. It is typically recommended patients suffer from spine instability, severe pain, or some form of deformity in the spine. Conditions that may necessitate spinal fusion include degenerative disc disease, spondylolisthesis, spinal fractures, spinal tumors and scoliosis [10]. The procedure involves joining two or more vertebrae together, which can be done through various techniques. These techniques often involve the use of bone grafts and metal implants (such as pedicle screws, rods, and plates) [15]. The targeted anatomical parts for fusion vary depending on the location and extent of the spinal condition. Spinal fusion surgery concerns the upper three sections of the spine. Namely the cervical spine (neck), thoracic spine (upper and middle back), and lumbar spine (lower back) these sections are shown in Figure 1.1a. The surgery can vary in scope depending on which part of the spine is affected.

In the cervical spine the procedure is performed to stabilize the neck, alleviate pain, and address conditions like cervical disc herniation, cervical spinal stenosis, or cervical degenerative disc disease. For the thoracic spine, fusion surgery aims to address spinal deformities, fractures, or tumors in the upper and middle back region. This typically involves fusing several vertebrae together to provide stability and correct spinal alignment. In the lumbar spine, fusion surgery is commonly performed to treat conditions such as degenerative disc disease, spondylolisthesis, or lumbar spinal stenosis. By fusing the affected vertebrae in the lower back, the surgery aims to reduce pain, improve stability, and restore normal spinal function .

Advances in surgical techniques, imaging technology, and instrumentation continue to improve patient outcomes and enhance the safety of these procedures [34]. Close attention to accurate screw placement and comprehensive surgical planning are vital to ensure successful outcomes in spinal fusion surgery.

### 1.1.3. Guidance during Spinal Fusion Surgery

Having proper guidance during spinal fusion surgery is crucial for ensuring accurate and safe outcomes. Incorrect placement of the pedicle screw can lead to serious trauma and patient discomfort. Figure 1.2 shows some examples of poorly placed pedicle screws [3]. These screws breach into the surrounding tissues, jeopardizing the integrity of the entire structure. Currently used clinical practices for pedicle screw placement vary from free-hand placement to 2-D fluoroscopy images and 3-D navigation planning systems [33]. These tools aid surgeons in real-time visualization of the patient's anatomy, allowing for precise screw placement, and optimal fusion alignment enabling a more minimally invasive surgery.

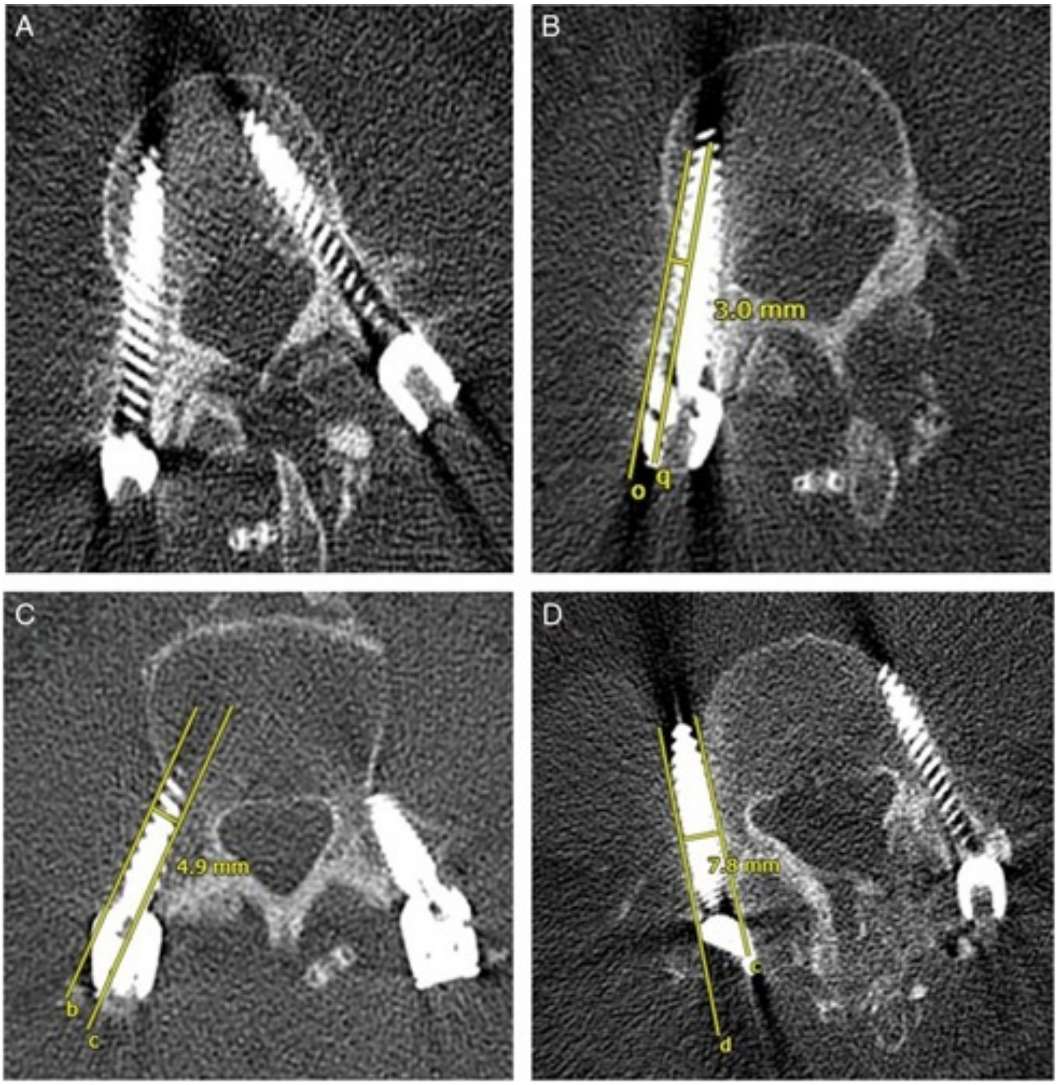


**Figure 1.2:** Examples of poor pedicle screw placements. (A) right-hand screw is entirely contained within the pedicle; while the left-hand screw has < 2mm pedicle breach; (B) < 4mm pedicle breach; (C) left-hand screw has < 6mm pedicle breach; (D) left-hand screw has ≥ 6mm pedicle breach. Figure adapted from [3].

A minimally invasive surgery enhance patient outcomes as patients report post-operative pain, fewer operative and post-operative complications, and faster recovery times [24]. While effective, these technologies often require expensive equipment, which can pose cost challenges for healthcare facilities and limit their widespread adoption. This together with the complex nature of the procedure cause the clinical outcomes to often depend on the surgeon's level of experience. There is great variability in the literature on the accuracy of screw placement ranging from under 30% to over 90% [23, 17].

To realize the benefits of a minimally invasive surgery, it must be performed through small incisions. This is only possible if guidance techniques are capable of compensating for the limited exposure of the surgical site [33]. For spinal fusion surgery this means the ensuring the guidance technology does not increase the size of the bone awl, the tool which will be equipped with the guidance technology. The bone awl plays a vital role in spinal fixation surgery as a specialized surgical instrument designed to prepare

the bone for the insertion of pedicle screws. During the procedure, the bone awl is utilized to create pilot holes or channels within the vertebral pedicles. These pilot holes serve as precise entry points for the placement of pedicle screws, essential for stabilizing the spinal segments during fusion [9].

## 1.2. Optical Spectroscopy

For a successful minimally invasive procedure, the surgeon must know where exactly the instruments are inside the body. When there is no direct line of sight, absolute information about the location of the instrument is difficult to acquire. Optical spectroscopy is capable of providing real-time information about the optical properties of the tissue surrounding the instrument and under the right conditions can differentiate between tissue types [31]. Without this information, a poorly placed pedicle screw may cause severe damage in the form of a breach into surrounding tissue or failure of the fixation. While some forms of optical spectroscopy require some form of tissue preparation, such as e.g. fluorescent markers to be used, other types such as Raman and DRS do not. This bears advantages as the tissues can remain in their respective natural states and no further tissue preparation is necessary [18].

In previous studies, Raman spectroscopy has been successfully used to asses bone quality. However, it has not yet been applied surgically which may be due to its acquisition time being up to two orders of magnitude higher than in other forms of spectroscopy [6]. Similar to Raman spectroscopy, DRS has shown to be capable of reliably sensing the optical properties in cancellous bone. This combined with its low acquisition time make it a viable optical sensing technique for use on a bone awl [6, 33, 32].

In summary, DRS is as a promising, cost-effective option to provide real-time guidance during pedicle screw placement. By integrating optical fibers into a bone awl, optical spectroscopy can be utilized to assess the characteristics, such as the scattering and absorption coefficients of the bone tissue in real-time and help reduce surgeon error. DRS offers the ability to measure light interactions with bone tissue, providing valuable information about how close a tissue with different optical properties may be. Additionally, DRS would not make the procedure more invasive, as the optical fibers occupy minimal space on the bone awl and not require an increase in diameter.

### 1.2.1. Diffuse Reflectance Spectroscopy

DRS is an optical sensing technique using at least one light-emitting (LE) and one light-collecting (LC) optical fiber. Only photons that are diffusely reflected by the medium under investigation will be collected by the LC fiber, hence the spectral information gathered is unique to each locally probed medium. Figure 1.3 shows some of the key optical phenomena involved in a DRS experiment [5]. Three main phenomena of light-tissue interaction are exploited by DRS [25]:

1. Elastic scattering occurs due to changes in the refractive index in the medium. It allows the photons to travel inside the tissue in all directions and to be partially back-collected at different points on the tissue surface after multiple scattering.

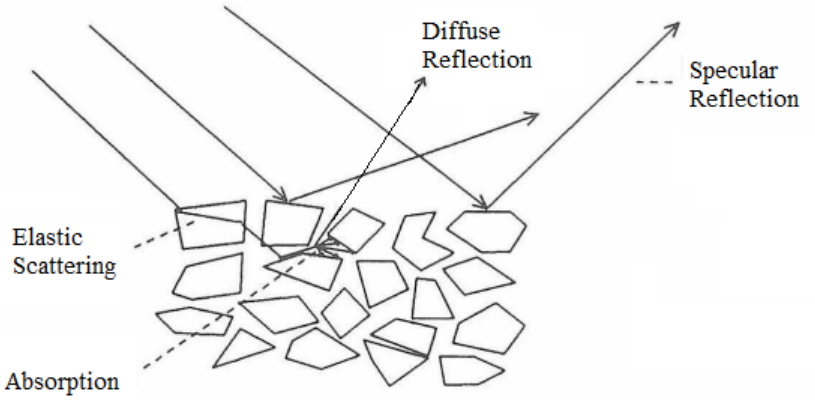


**Figure 1.3:** Different potential trajectories of photons as they meet an opaque solid medium (Figure adapted from *Blitz el al.* [5]) Photons which are not reflected will penetrate the surface and be either elastically scattered or absorbed. Scattered photons are ultimately absorbed, reflected or transmitted through the medium.

2. Absorption by intrinsic chromophores (e.g. water, melanin and haemoglobin) without re-emission *i.e.* a non-radiative process.
3. Absorption by intrinsic fluorophores (e.g. collagen, elastin, nicotinamide adenine dinucleotide and flavin adenine dinucleotide) followed by radiative emission of fluorescence.

The diffused photons can be received by a LC optical fiber and transported to a spectrometer. The spectrum of the light received by the spectrometer can be used to draw conclusions about the medium which the photons were internally reflected by [30]. In this context this information could be used to know how imminent a breach of the cortical bone may be.

The design of the DRS probe has a great influence on which information can be gained from the procedure. In broad terms, four main characteristics must be taken into consideration when designing a probe:

- **Number of Fibers used**
  More than one photon emitting and/or receiving fiber can be used. This will greatly influence the volume probed, as with more fibers, collected photons may have travelled through more sections of the probed medium.
- **Source-to-Detector Separation (SDS)**
  The SDS is defined as the distance between the photon emitting fiber and the photon receiving fiber. The greater the SDS, the greater the overall detection depth, as more photons will have traveled further into the tissue. The sampling depth, (also referred to as 'look ahead distance' or 'detection depth') is the maximum distance at which the signal-to-noise ratio is great enough to assess the sampled tissue [11]. Figure 1.4 is a visual representation of how varying the SDS affects the trajectory of the collected photons using the example of a tumor model.
- **Optical Fiber Diameter**
  The fiber diameter will affect at which rate photons are emitted and/or collected. Additionally, the greater the diameter of the light emitting fiber, the greater area

through which the photons first penetrate the medium. Furthermore, the greater the diameter of the photon receiving fiber, the greater the area over which photons are recollected meaning a greater volume is probed.

- **Wavelengths used in Light Source**
  The light source chosen (*i.e.* the wavelengths of the photons leaving the LE fiber) need to be strategically selected for each application. Photons of different wavelengths interact differently with different molecules. Ideally a spectrum of light is chosen which displays peaks or troughs in the measured spectrum, as this facilitates interpreting the data.

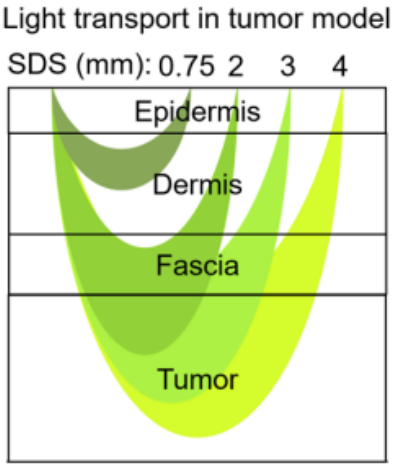


**Figure 1.4:** Influence of Source-to-Detector Separation (SDS) on Sampling depth. The greater the separation, the further into the sampling tissue the collected photons have travelled. (Figure adapted from [11]).

All these parameters must be considered collectively, not individually, *e.g.* assuming a probe tip is constrained in size, selecting optical fibers with a large diameter means that the SDS will be limited. Conversely selecting very small fibers limits the number of photons which will be collected. This could be solved not only by increasing the fiber diameter, but alternatively by changing the exposure time of the light source allowing more photons to reach the collecting fiber. Ultimately, researchers need to optimize the design of the DRS probe tip for each application.

### 1.2.2. Research Project at TU Delft

The unique build of the vertebrae provides additional challenges to spinal fusion surgery. As shown in Figure 1.1b the vertebrae consists of an inner core with cancellous bone and an outer layer of cortical bone. Cancellous bone is significantly less dense and stiff than cortical bone. Increasing the contact area between the pedicle screw and cortical bone therefore would improve the integrity of the fixation [29]. A pedicle screw solely anchored in cancellous bone may cause the patient issues later, as human bone density degrades naturally with age and elderly patients with osteoporosis may experience screw loosening [27]. With this in mind, a research group at TU Delft is developing a steerable bone drill with the ability to precisely drill along the interface of the cortical and cancellous bone to maximise the contact area between the pedicle screw and cortical bone [33]. However, drilling near the cortical bone bears risks, such as the breaches discussed in section 1.1.3. The outcomes of this study contribute to this

project, as a bone awl with DRS which is capable of providing guidance to surgeons has similar design considerations like a bone drill. The tissues they are operating on are the same and the shape of the medical instrument is also very similar (needle-shaped).

### 1.2.3. Considerations for DRS on a Bone awl

When considering using DRS on bone awls, the impact of the geometry of the bone awl must be considered with the characteristics mentioned in Section 1.2.1. The needle tip of the bone awl means the LC fiber will protrude further into the tissue than the LE fiber. The exact geometry of the probe will be further defined in Chapter 2.

When selecting the appropriate light spectrum, the optical properties of the illuminated tissue must be considered. Due to its biological functions, cancellous bone consists of more fat lipids than its neighboring tissues in the spine, namely cortical bone, muscle and nervous tissues. Fat chromophores, which are present in the lipids of cancellous bone, have a prominent peak in the absorption of light at wavelength of $1211nm$ [33]. As a consequence, tissues with higher lipid content exhibit a dip in the intensity of recollected light at $1211nm$. To leverage this unique optical property, the light emitted and collected by the probe should should have wavelengths in the near-infrared spectrum (NIR).

## 1.3. Goal of Thesis

The primary goal of the study is to understand how DRS, when integrated into a bone awl, would perform as a guidance aid to surgeons during pedicle screw placement. This is investigated using Monte Carlo simulations, experimental validation, and comparison of results, this thesis aims to provide a comprehensive understanding of the performance of DRS integrated into a slanted-tip bone awl. The outcomes of this research have the potential to contribute to the development of bone awl which provides real-time feedback about breach detection, thereby providing a low-cost alternative to current guidance aids for pedicle screw placement.

## 1.4. Structure of Thesis

Including this introduction chapter, this study consists of four chapters that collectively contribute to advancing our understanding of DRS in the context of varying protrusions.

Chapter 2 utilizes a numerical simulation tool perform Monte Carlo simulations for the propagation of light in cancellous bone tissue. These simulations predict the paths taken by photons as they travel from a LE fiber to a LC fiber. The simulations are performed multiple times at varying protrusions of the LC fiber to the LE fiber. This chapter aims to explore the impact of different awl geometries on the paths taken by recollected photons.

Chapter 3 presents an experimental validation study. A physical probe is designed and manufactured to perform DRS measurements in optical phantom bone. The probe can vary the protrusion of the LC fiber to the LE fiber, thereby simulating bone awls with tips of varying slopes. This chapter aims to validate the previously

obtained simulation results and provide empirical evidence of the probe's performance.

Chapter 4 provides a discussion and conclusion about the findings. The implications of the research findings and insights into the feasibility and potential of integrating DRS into a slanted-tip bone awl as a guidance aid for surgeons are discussed.

# 2

# Numerical Simulation of Photon Paths with varying Protrusions

## 2.1. Introduction

The purpose of using DRS in a bone awl is to provide the performing surgeon with guidance during spinal fusion surgery. This combination has the potential to provide real-time information about the location of the bone awl tip to surgeons. The primary objective of this chapter is to investigate and understand the impact of the bone awl's geometry on the efficacy of DRS as a guiding tool. More specifically, the influence of awl sharpness, i.e. the slope of the needle tip on DRS performance will be assessed. As elaborated upon in Section 1.1.3, bones awls can vary in how sharp their tip is. The placement of the LC fiber at the center of the needle allows for the potential collection of photons which have travelled the furthest into the tissue, i.e. the detection depth is maximized. A bone awl configured with optical fibers for the use of DRS in a surgical setting would have multiple LE fibers. This would have the key advantage of illuminating a greater volume of bone area and therefore provide an improved guidance for the surgeon. For the purposes of this study, only one LE fiber and LC fiber will be considered. This is because the photon paths taken by an additional LE would mirror those of the paths taken by the photons from the first LE fiber. Therefore if a DRS system can be shown to work for this simplified system, it can be assumed to work at least as well if more LE fibers were present.

To simulate different tip sharpness, the slope from the needle tip is considered, as shown by angle $\alpha$ in Figure 2.1. Given the variability observed in bone awl tip morphologies, this study will run simulations to assess DRS performance across diverse slope configurations ranging from 0° to 60° in 10° increments.

$$\alpha = \{0°, 10°, 20°, 30°, 40°, 50°, 60°\} \tag{2.1}$$

As discussed in Section 1.2.1, the SDS plays a major role in the detection depth achieved. When choosing a SDS, the optical properties of the tissue at hand are very important, as a larger SDS means the SNR suffers. Based on previous works in which DRS was used on bone tissue, a SDS of $1.41mm$ is chosen. At this distance previous works have achieved a good signal strength and found that DRS was capable of discerning between cancellous and cortical bone tissue [32]. As explained in Section 1.2.3, this was

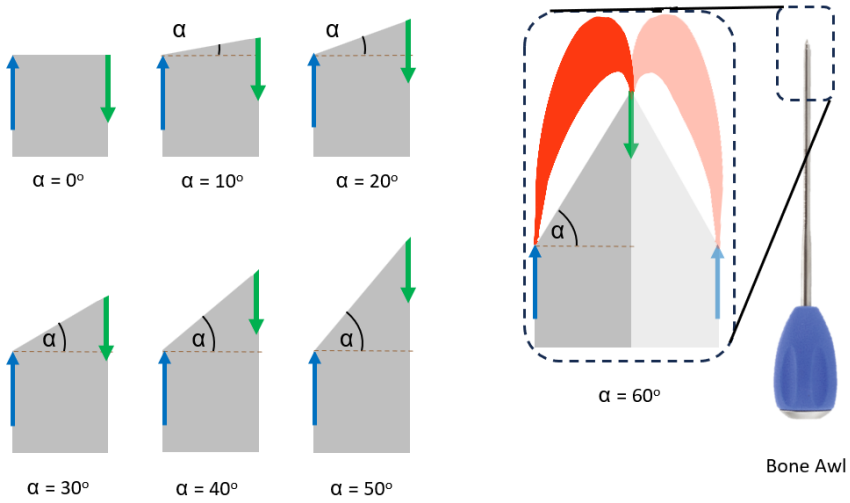


**Figure 2.1:** Needle Tips to be investigated. Seven configurations varying degrees of needle sharpness are defined for this study. The LC Fiber (in green) will protrude the LE fiber (in blue) on slopes with $\alpha$ ranging from 0° to 60° in 10° increments with a constant SDS of $1.41mm$. In red, a bananashape to represent an approximate path most recollected photons are expected to take. In this study only two optical fibers will be used in each configuration.

possible because of the pronounced light absorption peak at approximately $1211nm$ found in cancellous bone.

To evaluate the performance of DRS in different configurations, the functional requirements and performance criteria must be defined. Table 2.1 breaks down which criteria are considered. The specific metrics used to measure the performance criteria will be defined in Section 2.3.2.

**Table 2.1:** Performance requirements used to evaluate DRS efficacy

| **Performance Criterion** | **Variable** |
|---|---|
| Greatest possible detection depth | Distance achieved by recollected photons, measured from LC fiber tip |
| Maximize Signal-to-Noise Ratio | Percentage of emitted photons which reach LC fiber |

It must be noted that the performance criteria only consider the effectiveness of the DRS on the tip of the bone awl, not the performance of the tip of the bone awl itself. This is further discussed in Chapter 4.

## 2.2. Goal

The goal of the simulation study described in this chapter is to understand how a fiber constellation with an increasingly protruded LC fiber affects the paths taken by recollected photons (referred to as 'banana-shape'). The simulations will be performed using the MCMatlab tool created by [22] and provide information about the detection depth and signal strength. These simulations provide a basis for understanding how protruding the LC fiber ahead of the LE fiber affects the area probed and contribute to the overall goal of investigating whether DRS is an effective technology in providing guidance to surgeons during spinal fusion surgery.

## 2.3. Method

### 2.3.1. MCMatlab - Monte Carlo Simulations

This study used the open-source numerical simulation tool MCMatlab [22] in MATLAB [14] to predict the path photons take when emitted and collected by fibers in a protruding configuration. MC, short for Monte Carlo, is a technique employed to simulate physical processes using a stochastic model [22]. Within tissue optics, the MC method is commonly employed to approximate the distribution of light within biological tissue. In this method, light is represented as photon packets that travels through a turbid tissue and undergoes randomized scattering and absorption events. The trajectory taken by the photon packet is determined by statistically sampling probability distributions for step size and angular deflection per scattering event.

This method has been implanted numerous times in different programming languages. In this study, the MCMatlab program was specifically selected due to its open-source nature, user-friendliness, and relatively efficient performance. MCMatlab is based on a general method for implementing the MC technique in computer code [26]. The method uses photon packets to simulate how light behaves when entering a turbid medium. An MC simulation is initiated by launching a packet of photons into the previously defined tissue cuboid. Variable step sizes are employed, determined by a probability density function, to approach this path. At each step, a random absorption or scattering event occurs. This means that as the photon packets propagate, a portion of the packet is absorbed while the rest is scattered. The fraction of absorption and scattering is determined by the absorption coefficient ($\mu_a$) and scattering coefficient ($\mu_s$) of the tissue, as given by the following formula [22]:

$$fraction_{absorbed} = \frac{\mu_a}{\mu_a + \mu_s} \tag{2.2}$$

The direction of scattering is determined by the Henyey-Greenstein phase function, which uses the scattering anisotropy ($g$) of the tissue [12]. This anisotropy is defined as the average cosine of the scattering angles ($cos(\theta)$), and is used to approximate the angular dependence of light scattering. The Henyey-Greenstein phase function incorporates a random variable ($\epsilon$), uniformly distributed between zero and one, to account for the angular scattering variability. Combining this random variable with the Henyey-Greenstein scattering anisotropy determines the scattering angle ($\theta$) of a photon packet, as described by the following formula [37]:

$$\cos\theta = \begin{cases} \frac{1}{2g}\left(1 + g^2 - \left(\frac{1-g^2}{1-g+2g\epsilon}\right)^2\right), & \text{if } g \neq 0 \\ 1 - 2\epsilon, & \text{if } g = 0 \end{cases} \tag{2.3}$$

The procedure is repeated, calculating the step size and establishing the new scattering angle after each scattering event. However, at each step, the weight of the photon packet decreases due a fraction of it getting absorbed. If the weight falls below a certain threshold, a roulette selection mechanism is employed to either extinguish or continue propagating the photon packet. If the photon packet becomes completely absorbed by the simulated cube, a new photon packet is initiated at the LE fiber. A flowchart of this process is provided in Figure 2.2. Throughout the process, reflection, transmission,

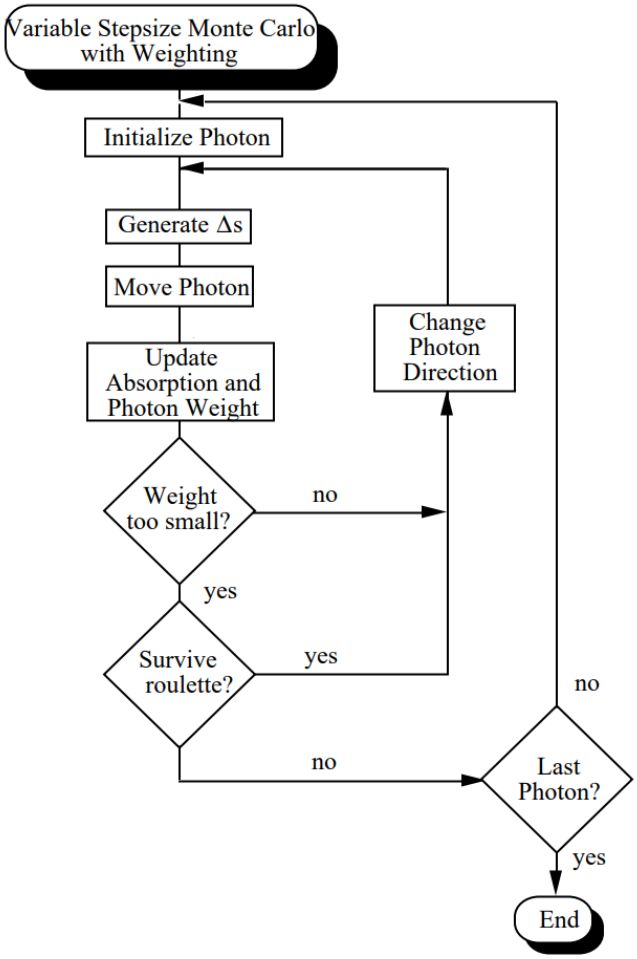


**Figure 2.2:** Flowchart for the variable step-size Monte Carlo technique. Photon packets undergo scattering and absorption events. With each absorption the weight of the photon packet reduces and eventually the photon packet is either completely absorbed, or exits the simulated cube. Figure modified from [26].

scattering, and absorption events are recorded for each photon packet. The results in this chapter represent the overall distribution of all paths taken by the recollected photons during the simulation. This is a very concise explanation of the MC method, which is employed in the MCMatlab application. A more comprehensive breakdown of the mathematical model, including examples of other applications for the model can be found in the respective literature [22, 26, 37].

### 2.3.2. Probe design (Simulations)

As mentioned, the MCMatlab model uses a cuboid to simulate the cancellous bone tissue. The larger the resolution of the cuboid, the more computational demanding the model becomes. To ensure the fewest number of photon packets which may reach

the LC fiber exit the cuboid prematurely, a larger cube was used for the larger fiber protrusions. The cuboid is defined to have the following dimensions:

$$V_{cuboid} = \begin{cases} 5\text{mm}*5\text{mm}*5\text{mm}, & \text{if } \alpha < 50° \\ 7\text{mm}*7\text{mm}*7\text{mm}, & \text{if } \alpha \geq 50° \end{cases} \tag{2.4}$$

Following this, the resolution of the cuboid is defined. Each pixel in the cube was set to be $10 * 10 * 10\mu m$ large. This is consistent for all $\alpha$.

The MC Matlab model does not allow for the fibers to be placed inside the cuboid. To combat this, both fibers are rotated by angle $\alpha$ for each slope. This means that, as shown in Figure 2.3, length $l$ must be defined as the distance between the tips of the fibers. This distance will be used in the simulations and be a proxy for changes in $\alpha$.

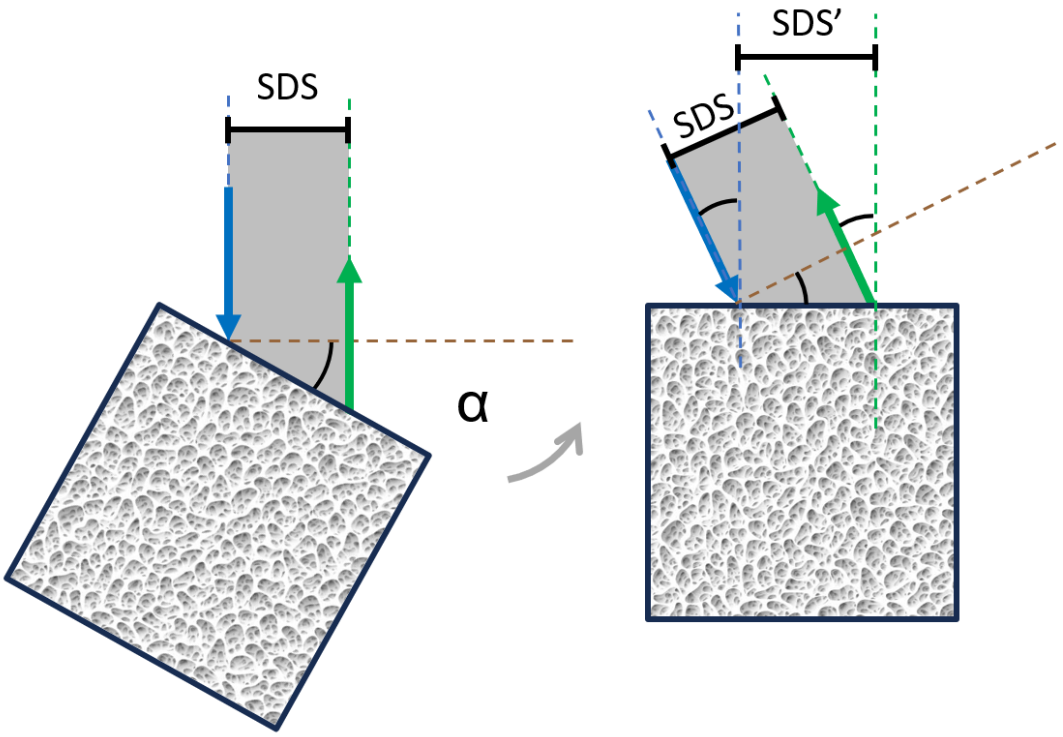


**Figure 2.3:** Visualization of the optical fiber arrangement in Simulations. The fibers are rotated by angle $\alpha$ to simulate the different fiber protrusions. Length $SDS'$ must be calculated and used at the distance between the fibers in the simulations. The LE fibers and LC fibers are shown in green and blue respectively. All indicated angles are equivalent to $\alpha$.

Distance $SDS'$ is therefore defined by the following formula to fully define the geometry of the model:

$$SDS' = \frac{SDS}{cos(\alpha)} \tag{2.5}$$

To represent the optical properties of cancellous bone tissue, the absorption coefficient ($\mu_a$) is defined as $1.422cm^{-1}$ and the scattering coefficient ($\mu_s$) is computed based on the reduced scattering coefficient ($\mu_s' = 19.5129cm^{-1}$ [33]) and computed using the following formula [22, 20]:

$$\mu_s' = \mu_s(1 - g) \tag{2.6}$$

All simulations were performed using $10^9$ photons at a wavelength of $1211nm$ as explained in Section 1.2.3. The detection depth will be measured starting at the LC fiber. The MCMatlab model does not account for noise, limiting the extent to which a SNR can be predicted in an experimental setting. However, previous studies using the same SDS and using a NIR spectrum on bone tissue have found a good SNR when the two fibers are parallel to each other at no slope [21]. Therefore, if the number of photons that reach light collector at a 0° slope will be used as a baseline for a strong SNR, and normalizing the data w.r.t. $\alpha = 0$ will allow for comparisons between the different $\alpha$ values.

Lastly, the optical fibers of the model are defined to have a diameter of $200\mu m$ and a numerical aperture of 0.22. The LE fiber is defined to be a Gaussian beam, meaning the photon packets leave the LE fiber in a Gaussian distribution. These values and definitions were chosen, as they are consistent with previous work using DRS on bone tissue [32] and are the same properties of the physical fibers which will be used in the experimental study in Chapter 3.

## 2.4. Results

The MCMatlab model yields 3D Models, which indicate the photons packets which have reached the LC fiber. Projected onto the xz-plane, a binary matrix is computed that displays the area which 68.3% of the detected photons pass through. Because it is a Gaussian distribution, this area accounts the mean photon path taken by all recollected photons within one standard deviation. This smoothens the shape of the banana-curves as outliers and unusual paths are eliminated and is shown in Figure 2.4. The images were rotated by their respective angle $\alpha$ to allow for a comparison of the banana-shapes. The LC fibers are aligned, as they represent the tip of the needle and the detection depth starting at the needle tip is of interest.

To quantify the detection depth achieved, the furthest point of the banana-shape from the LC fiber in the z-direction is measured. Figure 2.5a shows a negative linear correlation between the depth reached and alpha increasing ($R^2 = 0.98$).

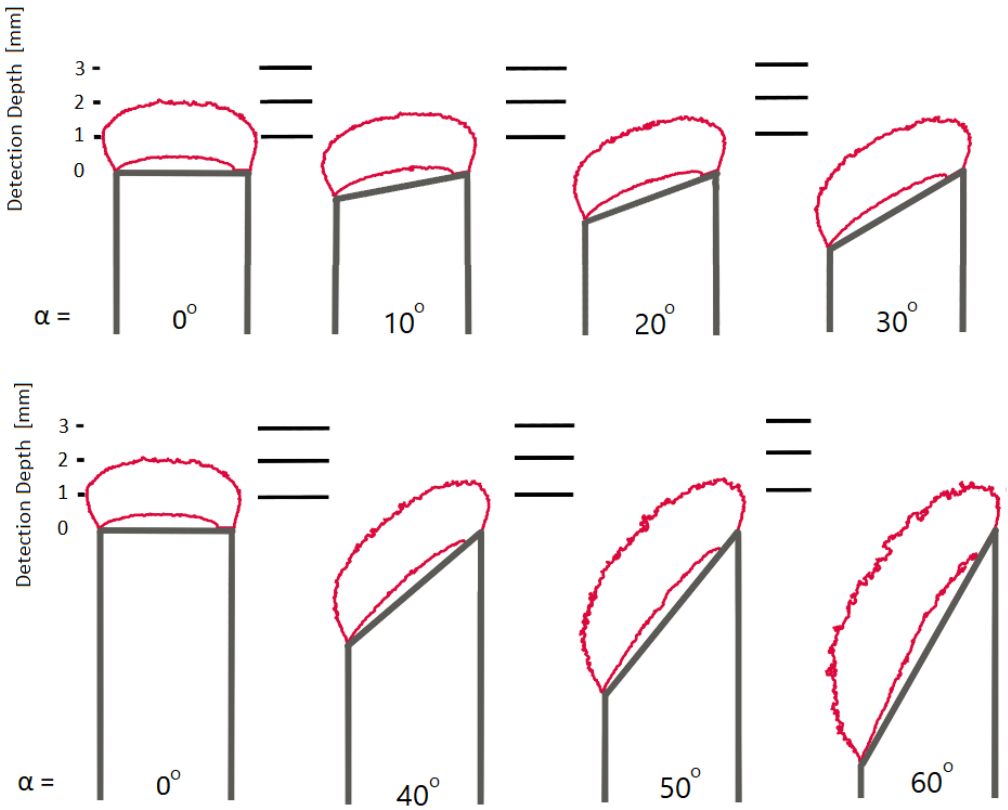


**Figure 2.4:** Visualization of all banana-shapes at different slopes. The red line displays the outline of the paths taken by 68.3 % of the photons which were collected at the LC fiber.

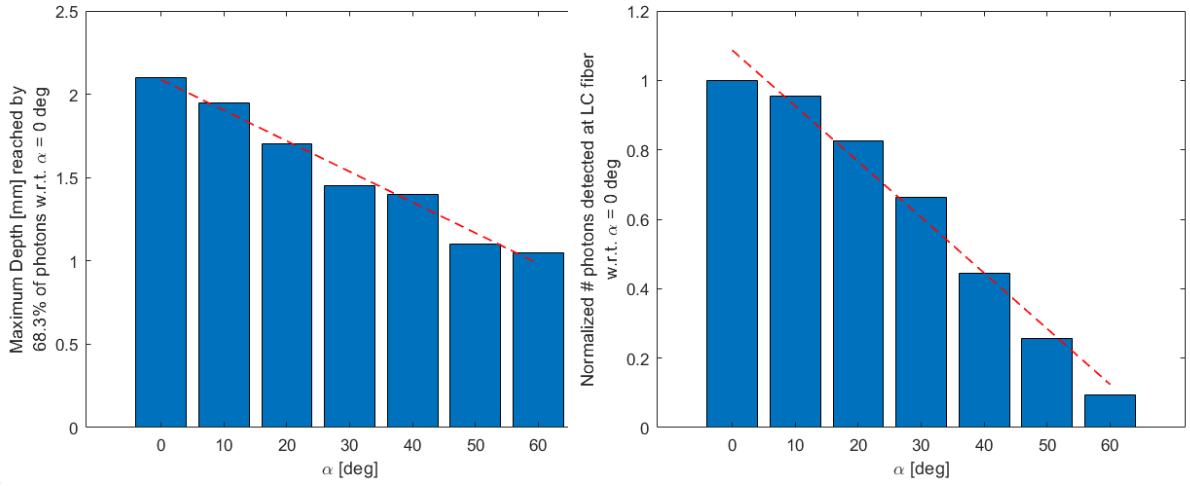


**(a)** Detection depth achieved by banana-shape containing 68.3% of photons packets detected at LC fiber for each $\alpha$ [deg]. The linear line of best fit has $R^2 = 0.98$.

**(b)** Normalized number of Photons detected at LC fiber for each $\alpha$ [deg] ($10^9$ photons emitted for each value of $\alpha$) The linear line of best fit has $R^2 = 0.97$.

**Figure 2.5:** Processed Results of MCMatlab simulations: Detection Depth and Signal Strength with respect to $\alpha$ [deg]

The results indicate, that all fiber constellations are able to reach a depth of at least

$1mm$. However, after the signal strength achieved is not sufficient for all $\alpha$. Figure 2.5b shows the clear negative linear relationship between the normalized number of photons that reach the LC fiber and increasing $\alpha$. The number of photons that reach the LC fiber falls below 50% of the signal strength when no protrusion is present.

To further understand how the signal strength changes with increasing $\alpha$, a logarithmic plot of the normalized fluency rate is created using a heatmap. This allows for a visual representation of paths taken by the detected photons (banana-shape) as well as the intensity of the light that reached the LC fiber. Figure 2.6 shows the logarithmic plots for all $\alpha$ values. It also shows that as $\alpha$ increases, the volume of the tissue probed increases, but the detection depth achieved and signal strength decrease. While the collected photons may still reach depths greater than $1mm$ as shown in figure 2.4, despite the intensity decreasing significantly. When $\alpha > 30^o$ the the normalized fluency rate between the fibers drops to the order of magnitude of $10^{-1}\ W/cm^2/W_{incident}$. At protrusions lower than this, the normalized fluency rate always reaches at least approximately $0.5 * 10^{-1} W/cm^2/W_{incident}$.

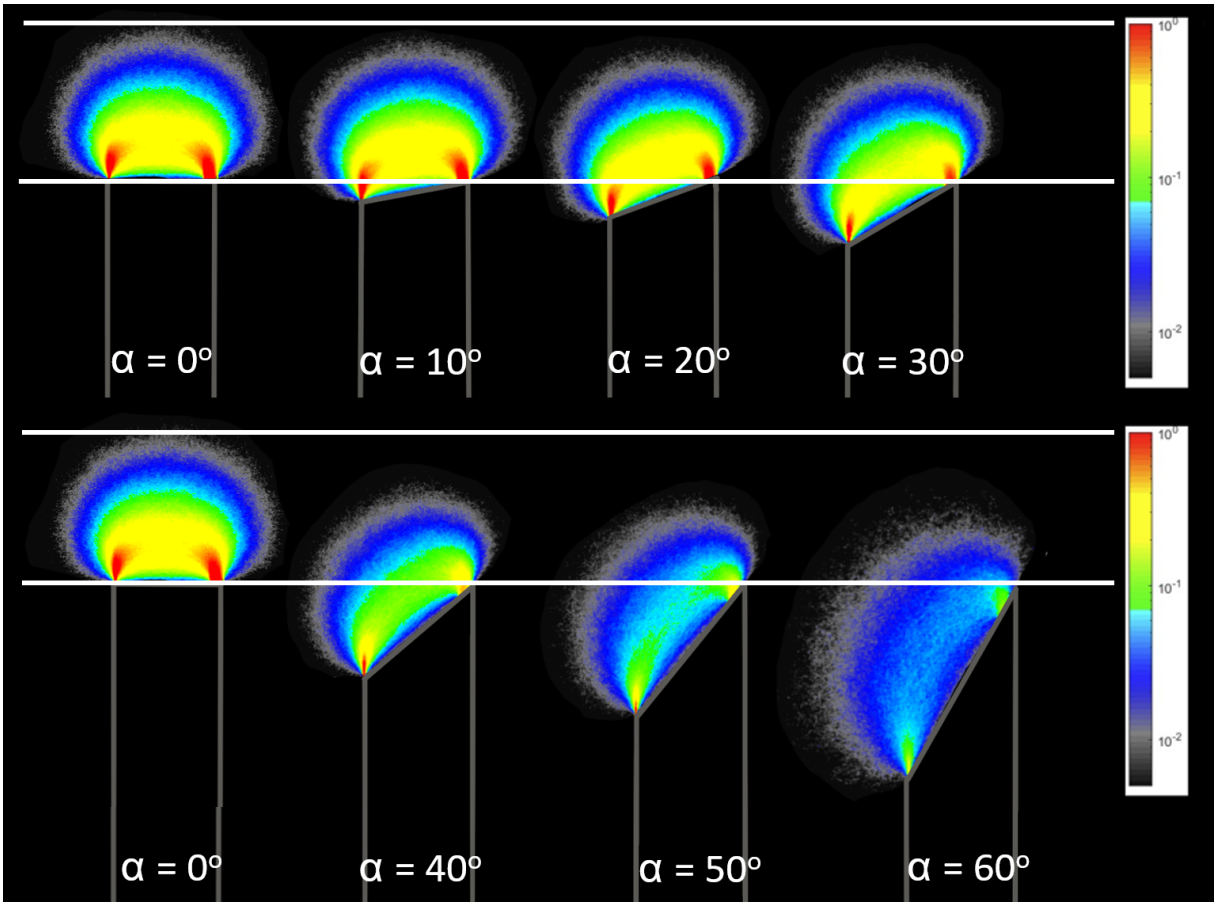


**Figure 2.6:** Normalized Fluency Rate of collected incident light [$W/cm^2/W_{incident}$] with increasing $\alpha$. The white lines align with the LC fibers and the maximum depth reached when $\alpha = 0^o$ for reference.

## 2.5. Discussion

### 2.5.1. Interpretation of Results

This study investigated the effect of the LC fiber protruding ahead of the LE fiber has on the path taken by recollected photons and what implications this has for potentially using DRS as a form of guidance in a bone awl. The performance was measured using two key indicators. The detection depth and the signal strength. Both have similar trends, but they do display key differences.

The detection depth is defined as the maximum depth achieved by 68.3% of the photons which reached the LC fiber. Using this method, the detection depth achieved was > 1 mm for all values of $\alpha$. However, the method of computing the detection depth does not adequately account for the deterioration in the number of photons which reach the LC fiber *i.e.* the signal strength. The heat-map presented in Figure 2.6 shows that although the few photons which reach the LC fiber probe a large volume of tissue, but noise levels, which were not simulated in this study would make the maximum detection increasingly less relevant.

The other key takeaway from the simulations is that the path the recollected photon take is consistently deep into the tissue. Protruding the LC fiber ahead of the LE fiber did not flatten the paths recollected photons take beyond the minimum required detection depth of 1mm. This suggests that if a good signal strength can be achieved in the experiments, good DRS performance may be possible at greater protrusions.

In previous work by *Swamy et al.*, an optical probe using DRS with an SDS of $1.22mm$ and no protrusion present achieved a detection depth of $1mm$ [33]. Since the SDS used in this study is slightly larger ($1.41mm$), a greater detection depth ($2.05mm$ when $\alpha = 0^o$) is consistent with previous works.

It is encouraging, that the photons which arrive at the LC fiber always penetrate into the tissue at least 1mm. This means that if the signal strength is sufficient, DRS should be able to determine the optical characteristics of the tissue investigated, also with protrusions present. Because of both the number of recollected photons and the normalized fluence rate dropping significantly after $30^o$, this value is considered the critical angle after which the performance of the DRS as a guidance deteriorates. The experiments in Chapter 3 will show if this critical angle holds true.

### 2.5.2. Limitations

The greatest limitation of the MCMatlab model is the lack of noise in the recordings. The model only accounts for photons that are emitted in a highly controlled environment and at a very precise wavelength. It is therefore uncertain whether DRS can reliably record a signal in an experimental setting with realistic noise levels present. The impact of the great reduction in recollected photons at larger $\alpha$ values cannot be fully understood through these simulations. Further investigation and experimentation will be necessary to understand these limitations before a bone awl using DRS can be used to provide guidance in a surgical setting.

Additionally, the computed detection depth may be slightly optimistic. This study considered the maximum depth to be the furthest point the simulated photon paths penetrate into the tissue (as shown in Figure 2.4). In an experimental setting with noise present, the true detection depth may differ.

## 2.6. Conclusion

In conclusion, the simulations demonstrate that the tested fiber arrangement can be used to illuminate cancellous bone tissue and could provide information about the potential tissue breach. While DRS performs optimally when no slope is present, the data still suggests that up to $30^o$ DRS can perform well in this new fiber configuration. The literature has suggested a detection depth of 1 mm is sufficient to provide the guidance during pedicle screw placement surgery [33], which is achieved by all configurations. The signal strength is the limiting factor, as the fluency rate and number of recollected photons fall significantly when $\alpha > 30^o$.

# 3

# Experimental study using customized Probe

## 3.1. Introduction

This chapter contains a design study in which a probe holding two optical fibers is designed and manufactured. The probe is used together with a spectrometer to investigate similar parameters presented in Chapter 2, namely the maximum detection depth and the signal strength for the same values of $\alpha$ ($0^o$ to $60^o$ in increments of $10^o$).

The spectrometer used contains an InGaAs detector (S330-2 NIR, HORIBA Scientific, Piscataway (NJ), USA) and can detect light in the NIR spectrum. Prior to measurements, the system was calibrated using a Spectralon white reference standard (WS-1-SL, Labsphere Inc., North Sutton (NH), USA). The same equipment was used and calibration procedures followed by the authors *Losch et. al.* [21]. Pure coconut milk from the brand "Go-Tan" and a fat content of 18% [1] will be used to simulate the optical properties of cancellous bone. Due to its fat content, coconut milk has been used previously to simulate the optical properties of cancellous bone tissue [19, 21]. The milk will be poured into a dish containing absorption tape at the bottom. All photons which reach the tape are completely absorbed have no chance of reaching the LC fiber. Hence the singal strength is expected to increase as the distance between the probe tip and the absorption tape increases. Once the signal strength reaches its maximum value, the maximum detection depth as been reached. These experiments help quantify the effect of an increasing protrusion on the detection depth and signal strength. The results of this study contribute to the understanding of the viability of using DRS as a form of guidance to surgeons when integrated into a bone awl.

## 3.2. Goal

The primary objective is to assess the impact of a protrusion of the LC fiber ahead of the LE fiber on the signal strength and detection depth in cancellous bone tissue.

To achieve this, a mechanism allowing for longitudinal displacement of the LC fiber is designed. A performance criteria is established to guide the concept designs, which are then evaluated using Harris profiles to determine the optimal mechanism for further

development. The selected design is modeled in Solidworks and 3D printed. After manufacturing and assembling the probe, experiments are conducted using a console which contains a spectrometer and a light source.

## 3.3. Designing of Optical Probe

### 3.3.1. Mechanism Selection

To achieve the most favorable outcome, a brainstorming session with TU Delft students from Industrial design, aerospace engineering and the mechanical engineer faculties was held. The sole prompt given to participants was the need of a mechanism capable of longitudinal displacing an optical fiber. Over a dozen different concepts were ideated. To move forward in the mechanism selection, the following functional requirements were defined:

1. Able to laterally displace an optical fiber, allowing for the protrusion of one fiber ahead of another.
2. Capable of repeatedly changing between different protrusions. This allows for the experiments to be conducted with the same probe, making more variables controlled.
3. Manufacturable through 3D printing.

After applying the functional requirements to the ideated mechanisms, three different concepts being selected for further consideration: A gate-lock mechanism, a conveyor belt system, and a pen-inspired mechanism. Figure 3.1 shows a sketch of the gate-lock mechanism. In Figure 3.1 (a) the LC fiber, shown in green, can be lifted and placed into one of the slots corresponding to a specific protrusion. The LE fiber, shown in blue is fixed in it's position on the frame. Figure 3.1 (b) contains the frontal view of the same mechanism and shows how a hand can grab the LC fiber. The sketches are not to scale.

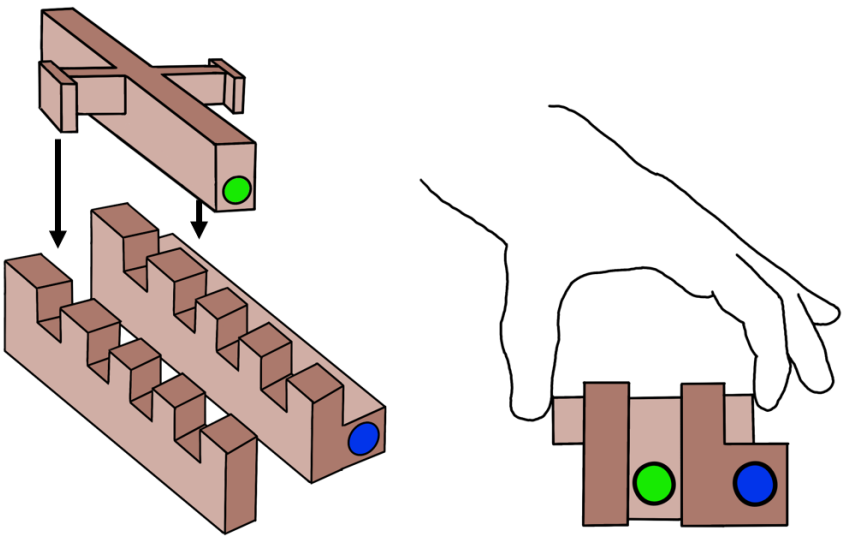


**Figure 3.1:** Sketch of the gate-lock concept. The position of the LC fiber (green) can be changed by placing it in a different slot on the frame. The LE fiber (blue) is fixed to the frame. Not to scale.

Figure 3.2(a) shows a sketch of the conveyor belt from the isometric view. The LC fiber (green) is attached to a conveyor belt. The LE fiber is fixed in it's position and does not move with the conveyor belt. Figure 3.2 (b) contains a side view of the mechanism. The LC fiber can be pushed forward (or pulled backwards), thereby changing how much is protrudes ahead of the LE fiber.

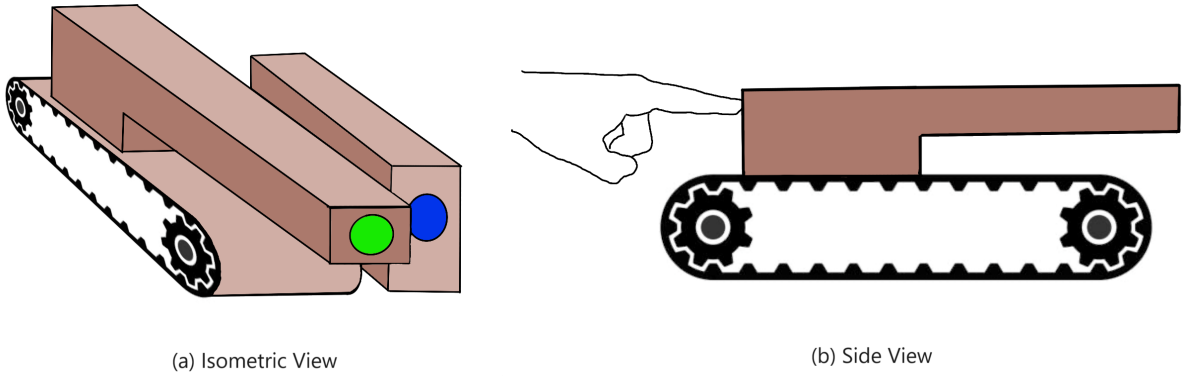


**Figure 3.2:** Sketch of the conveyor belt concept. The LE fiber (blue) is fixed in its position. The LC fiber (green) is attached to a conveyor belt and its position can be manipulated by pushing it along the conveyor belt, as shown in (b). Not to scale.

Finally, Figure 3.3 below present the pen-inspired mechanism. The LE fiber (blue) is glued to the main frame and does not move. The LC arm holds the LC fiber (green) and determines the position of the LC fiber. It is wedged between the spring and the cylinder. The spring pushes the LC arm into one of the cavities on the cylinder. To change the protrusion, the LC arm is pushed against the frame, compressing the spring. The cylinder can now freely rotate to a different position. Once the desired position is achieved, the LC arm is released causing the spring to push the LC arm into place again.

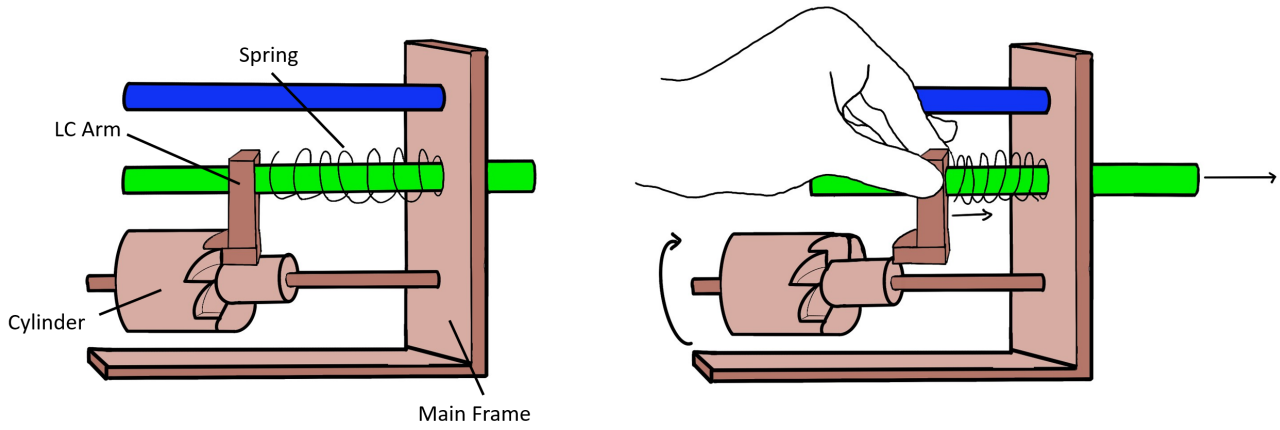


**Figure 3.3:** Sketch of the pen-inspired mechanism. The LE fiber (blue) is glued to the main frame. The LC arm is attached to the LC fiber (green) and is pushed into one of the cavities on the cylinder by a spring. To change the position of the LC fiber the LC arm is pushed towards the main frame, allowing the cylinder to be rotated into a different position. When the LC arm is released the spring pushed the LC arm back against the cylinder. Not to scale.

To facilitate a systematic evaluation of the three concepts, a Harris profile is created to select one for further development. The Harris profile highlights the relatively best and worst qualities of each concept. To achieve this, when scoring the concepts more weight is given to characteristics deemed crucial to the function or feasibility of the concept. Other factors, particularly those which may be considered 'nice to have' are given a lower weight score. The criteria considered in the Harris profile include the following:

1. **Able to achieve Accurate Position:** *weight = 2*
   Assess the capability of each concept design to accurately move to a specific protrusion. (Ranging from 0mm to 3mm, smallest increment is 0.25mm)
2. **Interchangeable between different protrusions:** *weight = 2*
   Consistently precise when repeatedly changing between protrusions.
3. **Ease of Use:** *weight = 1*
   Simplicity of changing between different protrusions.
4. **Manufacturability:** *weight = 1*
   Feasibility of manufacturing each design using 3D Printing technology.
5. **Ease of Assembly:** *weight = 1*
   The ease and efficiency of assembling each concept design.
6. **Mechanism Complexity:** *weight = 0.5*
   Relative complexity between the concepts. Factors such as number of parts required are considered.

Each criterion in the profile was rated on a scale ranging from $-2$ to 2, where a score of $-2$ indicated poor suitability and 2 indicated an excellent fit for the specific criterion. This score is then multiplied with the weight of each criterion, allowing for a more objective and systematic comparison. Tables 3.1, 3.2 and 3.3 show the Harris profiles for the conveyer belt concept, gate-lock mechanism and pen-inspired mechanism respectively.

**Table 3.1:** Harris Profile for Concept Design 1: Conveyer Belt Design

| **Criteria** | Weight | **-2** | **-1** | **1** | **2** | **Score** |
|---|---|---|---|---|---|---|
| Ability to Achieve Accurate Position | 2 | | | | | -4 |
| Replicably Precise | 2 | | | | | -2 |
| Ease of Use | 1 | | | | | 2 |
| Manufacturability | 1 | | | | | 2 |
| Ease of Assembly | 1 | | | | | 1 |
| Mechanism Complexity | 0.5 | | | | | 1 |
| **Total Score** | | | | | | **0** |

Table 3.1 shows the results for the conveyor belt design. It is a very simple concept and very easy to manipulate. The outstanding weak point is its ability to achieve an accurate position. While certain precautions can be made to mitigate this, such as the implementation of springs and gears of varying sizes, this would significantly increase the mechanism complexity and affect its manufacturability.

**Table 3.2:** Harris Profile for Concept Design 2: Gate Lock Mechanism

| **Criteria** | Weight | **-2** | **-1** | **1** | **2** | **Score** |
|---|---|---|---|---|---|---|
| Ability to Achieve Accurate Position | 2 | | | | | 2 |
| Replicably Precise | 2 | | | | | 2 |
| Ease of Use | 1 | | | | | 2 |
| Manufacturability | 1 | | | | | -1 |
| Ease of Assembly | 1 | | | | | 1 |
| Mechanism Complexity | 0.5 | | | | | 1 |
| **Total Score** | | | | | | **7** |

For the gate-lock mechanism, Table 3.2 highlights that the key benefits of the mechanism are its simplicity and its ease of use. However, its biggest flaw is its poor manufacturability. The distance the optical fiber is displaced by between trials is as low as 0.25mm making it difficult to manufacture the mechanism in a way which is stable if some key structures are so thin. Additionally, similar to the conveyer belt concept, its accuracy is limited as there will always be some play in each slot.

**Table 3.3:** Harris Profile for Concept Design 3: Pen mechanism

| **Criteria** | Weight | **-2** | **-1** | **1** | **2** | **Score** |
|---|---|---|---|---|---|---|
| Ability to Achieve Accurate Position | 2 | | | | | 4 |
| Replicably Precise | 2 | | | | | 4 |
| Ease of Use | 1 | | | | | 1 |
| Manufacturability | 1 | | | | | 1 |
| Ease of Assembly | 1 | | | | | -1 |
| Mechanism Complexity | 0.5 | | | | | 0.5 |
| **Total Score** | | | | | | **8.5** |

The pen-inspired mechanism, shown in Table 3.3, received the highest overall score when applying the Harris profile. While it is not as simple as the other designs, it excels in being replicably precise and can achieve an accurate position repeatedly. It does require a more elaborate design and manufacturing process, but the ability to accuracy and replicability make it worth it. The pen-inspired concept is selected for further development of the optical probe.

### 3.3.2. Final Design

With the pen-inspired mechanism, a cylinder with cavities for the arm holding the LC fiber is pushed back against needs to be be designed. The placement of these cavities depends on the distance the LC fiber protrudes ahead of the LE fiber. This distance is defined as length $l$ in Figure 3.4 and depends on the value of $\alpha$.

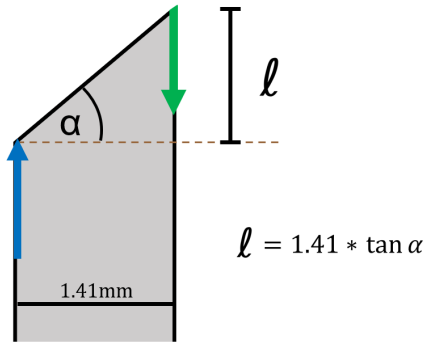


**Figure 3.4:** Geometry of distance $l$ relative to $\alpha$. The blue and green arrows correspond to the LE and LC fibers respectively.

Using this relationship, the exact protrusions are calculated and used in the design on the cylinder. The values of $l$ and the corresponding values of $\alpha$ are shown in Table 3.4 below.

| $\alpha$ | $l$ [mm] |
|---|---|
| 0° | $0.000mm$ |
| 10° | $0.248mm$ |
| 20° | $0.513mm$ |
| 30° | $0.814mm$ |
| 40° | $1.183mm$ |
| 50° | $1.680mm$ |
| 60° | $2.440mm$ |

**Table 3.4:** Protrusions for each $\alpha$ expressed in $l[mm]$

With the key dimensions calculated, the mechanism was designed using Solidworks [7]. Figure 3.5 shows the core of the mechanism. The LC arm has the LC fiber running through it. The main frame has the LE fiber glued to it and a hold cut out for the LC arm to move freely through it. To change the position of the fiber, the LC arm is pushed forward into the main frame, compressing the spring. This allows for the cylinder to freely rotate to a different protrusion setting. When the cylinder has been rotated to the desired setting, the LC arm can be released. The spring will push the arm into a different cavity on the cylinder and hold the mechanism in place.

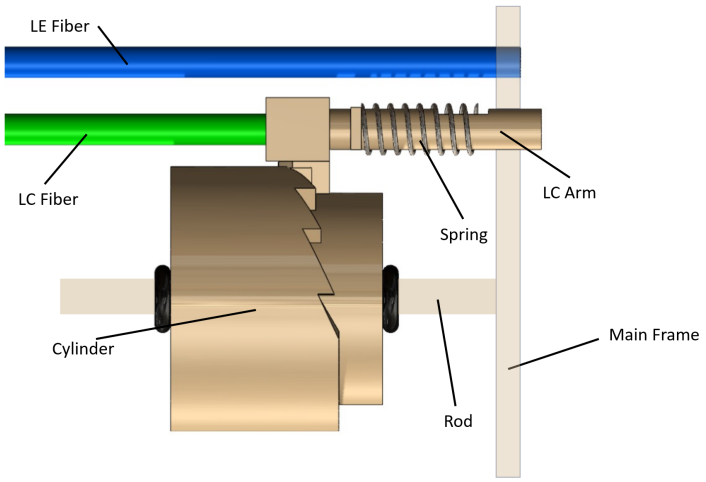


**Figure 3.5:** Rendering of the core mechanism. The LE Fiber (blue) is glued to the Main Frame. The LC Fiber runs through the LC arm. A spring pushes the LC arm into one of the cavities of the cylinder, corresponding to the different values of $\alpha$.

The mechanism allows for the position of the LC fiber to be changed repeatedly, facilitating the data acquisition. During the prototyping of the mechanism, it was discovered that the optical fibers are quite delicate. To avoid any damage to the fibers, particularly during transport, support structures were added. Additionally, the final design includes an adapter to facilitate screwing the probe onto the micro-stage and some supports to hold the optical fibers in place. Following Figure 3.6 which shows the entire probe.

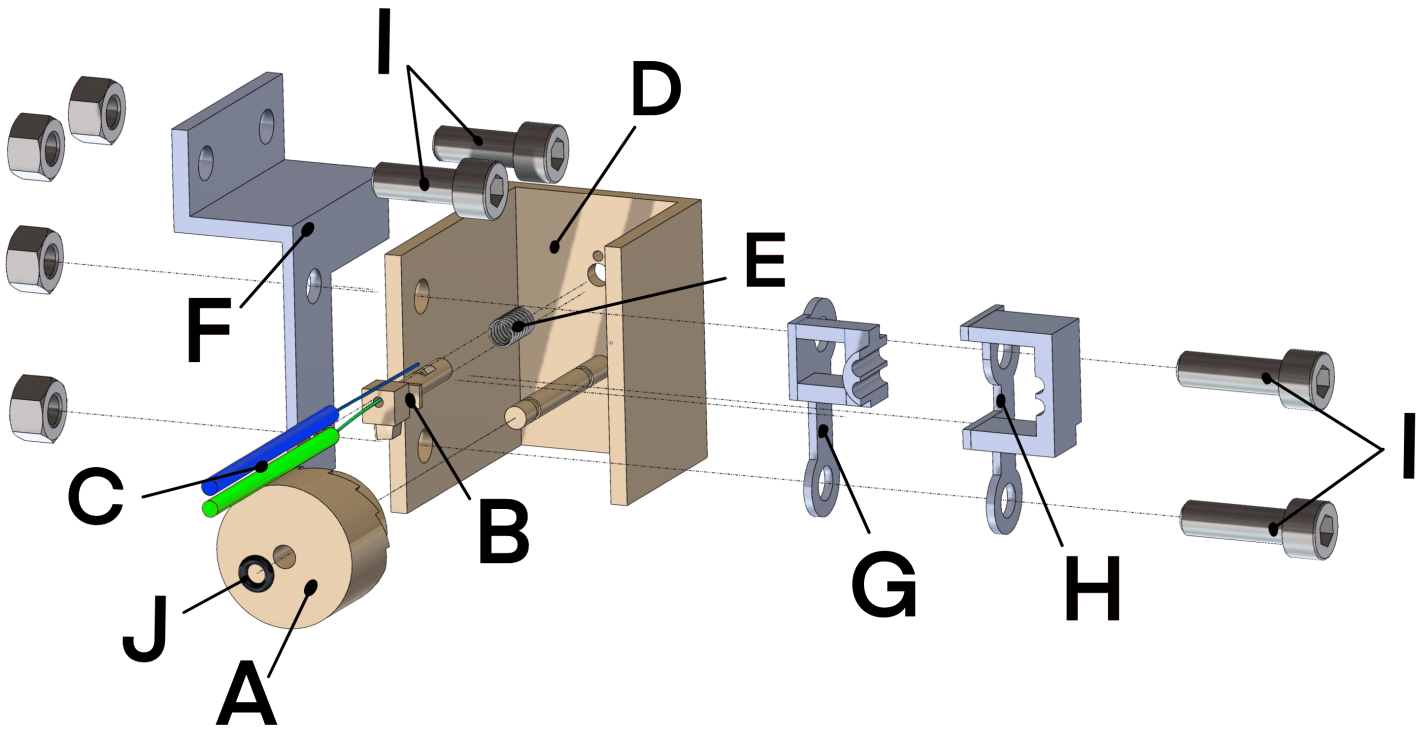


| Part | Name | Part | Name |
|---|---|---|---|
| A | Cylinder | F | Adapter |
| B | LC Fiber Arm | G | Fiber Support I |
| C | Optical Fibers (LE in blue, LC in green) | H | Fiber Support II |
| D | Main Frame | I | M6 screw |
| E | Spring | J | Insulation Ring |

**Figure 3.6:** Final design used in experiments, including all supports and screws used. The LE fiber (blue) is glued into the Main Frame (D) and then LC fiber (green) runs through the LC fiber arm (b) and has a dedicated hole in the Main Frame.

### 3.3.3. Experimental Set-up

In this experiment, the designed probe was securely fixed onto a linear microstage [2], which in turn was mounted on a vertically fixed breadboard. The microstage allowed for manual vertical adjustments in precise $0.25mm$ increments. To create a consistent and controlled setup, a plastic dish was prepared with black light absorption tape affixed to the bottom. Following this, the coconut milk [1], serving as the simulated tissue medium, was carefully poured into the dish. The probe was set to the desired slope and gradually lowered until the LC fiber gently touched the black tape at the dish's base. A picture of the set-up was taken and is shown in Figure 3.7.

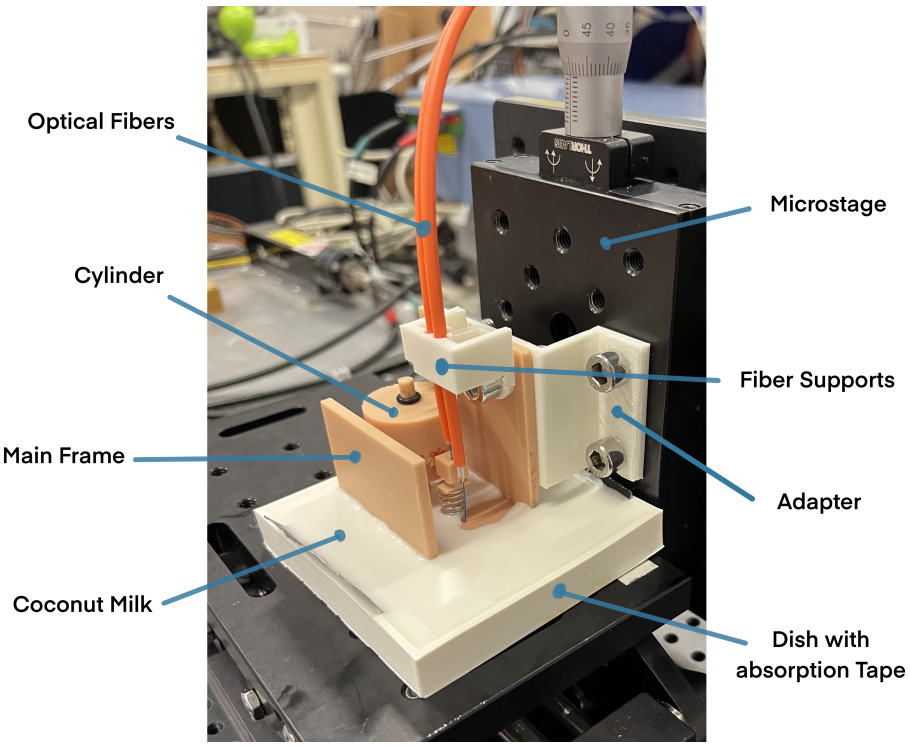


**Figure 3.7:** Picture of the probe during testing

The experiment involved systematically measuring reflectance data at various distances between the LC fiber and the absorption tape. At each distance, ten reflectance measurements are recorded using the spectrometer. At each measurement, light with wavelengths 900nm - 1700nm is emitted and collected. The integration time is set at 1000ms. After each measurement the microstage, along with the probe, is raised by $0.25mm$ to increase the distance between the LC fiber and the black tape. This process was repeated until a distance of 3mm between the absorption tape and LC fiber was reached.

The experiment was performed for each specified angle $\alpha$, allowing for an evaluation of the probe's performance with different awl sharpness'. To ensure reliability and minimize potential irregularities, the entire procedure was repeated three times, with fresh pieces of absorption tape and coconut milk used in each repetition. This means that for every angle $\alpha$ and each LC fiber to black tape distance, 30 measurements were taken, improving the replicability of the collected data.

## 3.4. Results

The output of the spectrometer is the measured reflectance spectra for all 210 measurements (30 measurements at 7 different $\alpha$). Before further processing was done, the highest and lowest reflectance spectra at each $\alpha$ at each distance between the LC and black tape is discarded, leaving 28 measured spectra per $\alpha$. This was done to eliminate any clear outliers. During the measurements it was observed that sometimes, the first measured reflectance spectra varied significantly from the rest of the measurements. Table 3.5 contains the average of 28 measured reflectance spectra for each $\alpha$ and at each distance from the LC to the black tape.

| | Distance from Probe Tip [mm] | | | | | | | | | | | | |
|---|---|---|---|---|---|---|---|---|---|---|---|---|---|
| Slopes | **0.00** | **0.25** | **0.50** | **0.75** | **1.00** | **1.25** | **1.50** | **1.75** | **2.00** | **2.25** | **2.50** | **2.75** | **3.00** |
| 0° | 7.05 | 10.73 | 15.51 | 18.70 | 20.47 | 21.44 | 21.95 | 22.19 | 22.30 | 22.39 | 22.47 | 22.52 | 22.49 |
| 10° | 3.42 | 6.46 | 11.90 | 16.02 | 18.53 | 19.92 | 20.75 | 21.14 | 21.29 | 21.48 | 21.51 | 21.57 | 21.59 |
| 20° | 4.34 | 8.35 | 13.42 | 16.86 | 18.92 | 20.01 | 20.62 | 20.95 | 21.17 | 21.22 | 21.31 | 21.37 | 21.38 |
| 30° | 5.70 | 8.80 | 12.86 | 15.34 | 16.75 | 17.53 | 17.94 | 18.19 | 18.27 | 18.32 | 18.35 | 18.38 | 18.38 |
| 40° | 6.00 | 8.59 | 11.56 | 13.13 | 13.96 | 14.47 | 14.71 | 14.83 | 14.92 | 14.95 | 15.03 | 15.10 | 15.10 |
| 50° | 4.88 | 6.65 | 8.21 | 9.02 | 9.43 | 9.64 | 9.78 | 9.79 | 9.83 | 9.87 | 9.89 | 9.86 | 9.87 |
| 60° | 3.00 | 3.95 | 4.77 | 5.21 | 5.44 | 5.53 | 5.59 | 5.63 | 5.64 | 5.65 | 5.64 | 5.65 | 5.67 |

**Table 3.5:** Measured reflectance Spectra ($\lambda_0$ = 1211nm). The experiment was conducted up to a distance of 0.300 cm. Cells in the table are dyed green when 95% of the maximum signal strength has been exceeded. This is used as a basis for calculating the maximum detection depth for each value of $\alpha$.

The table shows that the measured intensity ($\lambda_0$ = 1211nm) collected at the LC fiber increased with every step until a plateau is reached. The table shows that as $\alpha$ increases, the magnitude of the measured intensity plateaus at a lower value. To investigate the intensity of the light reaching the LC fiber, the intensities taken at 3.00mm are considered. The intensities of all measurements have plateaued at this point. The values are then normalized to the intensity measured at 0 degrees *i.e.* when there is no protrusion of the LC fiber. Figure 3.8 shows the relationship between this normalized intensity and the increasing slope between the fibers. The measured intensities decrease with every increase in slope. The $R^2$ value of the linear relationship is 0.91. However, up to a slope of 20°, the intensity of the collected light is within one standard deviation of the maximum when $\alpha = 0°$, suggesting the performance of the optical probe only marginally deteriorates at small protrusions.

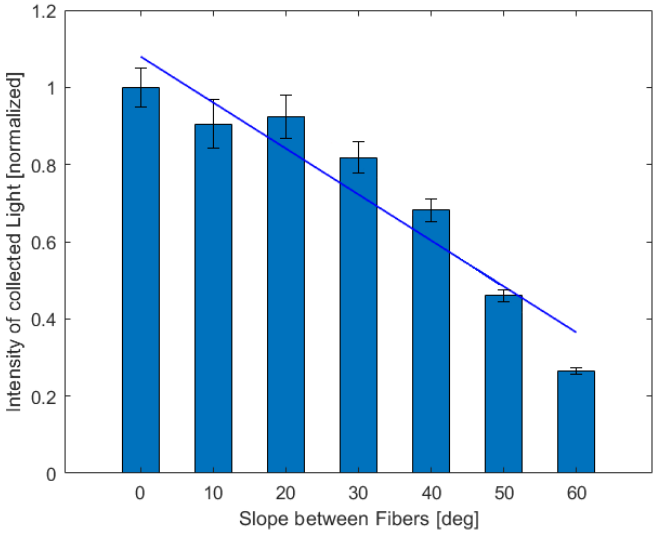


**Figure 3.8:** Collected Intensity measured at 2.25mm and normalized to $\alpha = 0$. $R^2 = 0.90$ and linear relationship is shown in blue.

The other key variable to evaluate the performance of DRS is the detection depth. To quantify and make relative comparisons between detection depth and $\alpha$, the point at which 95% of the maximum signal strength has been achieved is considered the detection depth. This relatively high value was chosen, because the difference in magnitude of the measurements varies significantly. As table 3.5 shows, the difference in intensity of the measured spectra for $\alpha = 0°$ is 7.05 at distance 0mm and 22.39 at 3mm. For $\alpha = 60°$ the measured intensities were only 3.00 and 5.67 respectively. For this a simple linear interpolation is performed and the results can be seen in Figure 3.9. The data shows the maximum detection depth was achieved when the slope between the fibers was $\alpha = 10°$. At subsequent higher values the distance at which 95% of the max signal strength is reached decreases in a near-linear relationship.

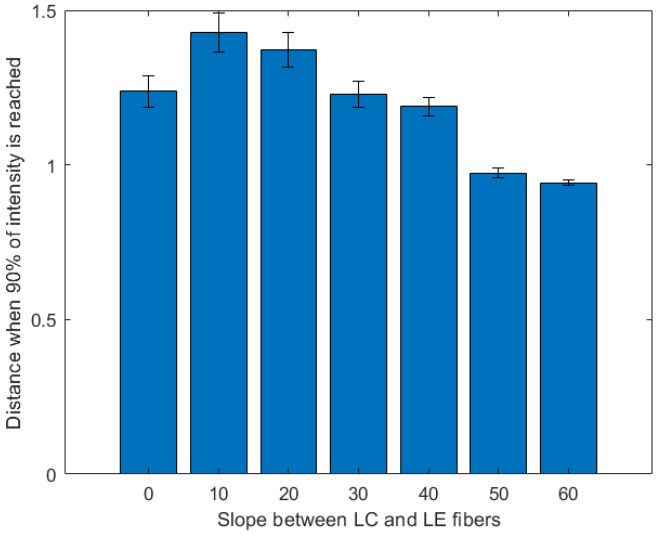


**Figure 3.9:** Distance between the probe and the black absorption tape when 95% of maximum intensity is reached.

## 3.5. Discussion

### 3.5.1. Interpretation of Results

This experimental study investigated the influence on DRS with an increased protrusion of the LC fiber on the signal strength and detection depth achieved. There are two key findings to consider from the collected intensities. Firstly, the relationship for signal strength was decreasing ($R^2 = 0.90$. This means that there is no indication that suggests the signal strength can be improved through the protrusion. Therefore when purely considering signal strength, the optimal configuration would be without any protrusion present.

The results also show that as the distance between the probe tip and the bottom of the dish increases, so does the intensity measured at the LC fiber. This trend is expected, because at small distances between the LE fiber and the black tape many of the photons which would have been internally reflected back to the LC fiber are completely absorbed by the black tape. The values in table 3.5 are inconsistent at very low distances. This is likely that because the dental resin used to print the probe is partially translucent and residue light could reach the LC fiber from the LE fiber without travelling through the coconut milk. This was only possible at small $\alpha$ values and the effects are negligible at greater distances between the LC fiber and black tape.

Despite the clear overall trend, it is important to note the signal strength remained within one standard deviation of the signal strength when no protrusion up until a slope of 20°. This suggests that DRS on a bone awl is likely to work without a significant loss of SNR on a bone awl with a tip sharpness up to 20°. This is supported by the linear relationship when only considering $\alpha \geq 20$ in Figure 3.8, which has $R^2 = 0.98$. The $R^2$ value for a linear relationship for all $\alpha$ is 0.90.

Crucially, the signal intensity falls below 50% of the intensity at $\alpha = 0^o$ when $\alpha > 40^o$. This was the same criterion used in Chapter 2 when defining the critical angle - the sharpest angle at which DRS can still perform well enough to provide guidance during surgery. The experimental findings therefore suggest the critical angle is $40^o$.

The other key finding concerns the detection depth, *i.e.* the relationship between the point at which 95% of the maximum intensity is reached for each $\alpha$. Here the relationship is not monotonous, as the detection depth increased from no slope, to a 10° slope. However, the apparent increase in detection depth does not account for the reduction in the signal intensity and it is likely both would achieve similar results in further testing. The detection depth remains above 1mm until $\alpha > 40^o$. It must be noted the SNR in the controlled setting of this study is likely much greater than in a real-world surgical setting. It therefore requires further testing in a less controlled, more realistic environment to understand at which angle $\alpha$ the SNR deteriorates too much to provide useful guidance during surgery.

When comparing the trends observed in both detection depth and signal strength, the rate of decrease in detection depth with larger values of $\alpha$ is lower than the rate loss in the intensity of collected light. This suggests that with an increasing

protrusion (increasing $\alpha$), the volume traversed by the photons does not decrease as quickly as the signal strength deteriorates. This is similar to the findings in chapter 2, where at greater protrusions the detection depth (in this definition) began to decrease.

In summary, the experiment showed that using DRS with a protrusion present good performance (Signal strength $I_\alpha$ > 50% of $I_\alpha(0)$ and detection depth > 1mm) results can be achieved up to a certain point. The results of this study suggest that this point is reached at protrusions greater than 40°. After this point, the signal has lost half of its intensity and considering this experiment was performed on a very homogeneous medium under perfect conditions, it is likely much more noise would be present in measurements taken during a surgery on human bone.

To better understand exactly at which point the signal deterioration becomes too significant for tissue classification, a more complex experimental set-up with realistic background noise levels present needs to be conducted. This would allow for a more definitive evaluation of the ability of DRS to perform guidance during pedicle screw placement. If the 'critical angle' is too low, the sharpest the needle of the bone awl could be is limited. If the reduced needle sharpness risks reducing patient outcomes or make it a less likely choice for surgeons, the viability of the using DRS on a bone awl needs to be re-evaluated.

### 3.5.2. Limitations

There are multiple drawbacks this study has which limit the impact of the results. The model used a highly simplified model. The cancellous bone is assumed to be perfectly homogeneous in terms of its optical properties. Additionally the optical properties of cancellous bone tissue is not identical to coconut milk. The fat content of 18% in the coconut milk is lower than in cancellous bone, suggesting in human cancellous bone the absorption of photons at wavelength 1211nm would be more pronounced and may affect the variables measured by the DRS. The detection depth may be lower than the true detection depth because of the simulated fat content.

Additionally, the model does not consider how the signal would be impacted by photons which reach the LC fiber after interacted with a bordering tissue. It is assumed that if a photon with wavelength $1211nm$ leaves the cancellous bone, it will not be reflected back to the LC fiber. This assumption is made, because no relevant surrounding tissue has a fat content comparable to cancellous bone, but it has not been experimentally validated.

Apart from model assumptions which can eventually be validated through *in-vivo* testing, other limitations of this study require further investigation. During the experiment, it was observed that the coconut milk would eventually begin to demulsify. Little clumps of fat would begin to congregate on the surface of the probe. Although the fat is part of the model and substances such as blood may also coagulate during the real procedure, these are not controlled phenomena and could impact the replicability results. In a future experimented this could be counteracted by adding a heating plate to the experimental design to control the temperature and delay the natural separation of components of coconut milk.

This experiment is also limited in how to quantify certain variables. The detection depth was defined as the point at which the signal intensity reached 95% of the maximum value for that fiber configuration. This does provide information about the paths the collected photons take (similar to the banana-shaped paths seen in Chapter 2), but it does not account for the absolute intensity of the signal.

Another relevant limitation in this study is the number of optical fibers used. As shown in Figure 2.1 the ultimate tip design would include at least one more light collecting fiber on the bone awl tip. The effect of multiple light collecting fibers has yet to be investigated. The impact could range from insignificant, to a potentially greater signal strength at greater needle sharpness' when compared to the two-fiber constellation considering in this study.

## 3.6. Conclusion

In conclusion, the experimental study finds that it is possible to use DRS in a constellation where the LC fiber is protruded ahead of the LE fiber to classify cancellous bone tissue. The results indicate the detection depth is greater than 1mm from $\alpha = 0$, up until a slope of $\alpha = 40^o$. Furthermore, the signal strength remained strong enough until $\alpha = 40^o$.

Hence, the experiments suggest that DRS can be used as a form of guidance even when adapted to the geometry of a bone awl (up to a needle sharpness of $\alpha = 40^o$) and the results open the opportunity for further research into the limitations brought forward. Specifically, further research into how the signal is affected when light which has penetrated into a surrounding tissue is collected by the LC fiber should to be investigated. Further research should also identify differences between cancellous bone and its surrounding tissues (connective tissue and cortical bone) to improve the signal interpretation.

# 4

# Discussion and Conclusion

## 4.1. Overall Findings

The work presented in this thesis provides a comprehensive exploration into the performance of DRS as a guiding aid to surgeons, when integrated into the tip of a bone awl. Specifically, the effect of an increasing protrusion of the LC fiber ahead of the LE fiber is investigated by measuring the detection depth and signal strength at varying degrees of protrusion. The protrusion corresponds to how sharp the device is.

A literature review into the currently used medical applications of DRS revealed a gap in knowledge about the performance of DRS when one fiber is protruded ahead of the other. To asses the optical properties of tissues during surgery, the sensing technique used often has to be able to work around the needle-shaped tips present on many surgical instruments.

Chapter 2 investigates the viability of DRS for this application. This is done using Monte Carlo simulations to predict the paths photons of wavelength 1211nm would take through cancellous bone. The results show a negative correlation between both the signal strength and increasing $\alpha$ as well as between the detection depth and increasing $\alpha$. Despite this trend, the detection depth and signal strength remain strong for all $\alpha \leq 30°$. At greater values of $\alpha$, the detection depth falls to about 1mm which is still above the minimum required depth of 1mm as elaborated in Chapter 1. Also past this point, the signal strength deteriorates to less than 50% of the signal strength when $\alpha = 0°$ (50% $I_\alpha(0°)$), and noise may begin to interfere with the readings.

Chapter 3 presents a design study, where the results of Chapter 2 were verified experimentally. To realize this, a mechanism which can accurately change the protrusion of the LC fiber is designed, prototyped and manufactured. Similar to Chapter 2, the results of the experiments yield a negative correlation between the signal strength and $\alpha$. The performance of DRS decreased with increasing protrusions, however, the decrease in performance was not greater than 50% $I_\alpha(0°)$ for all $\alpha \leq 40°$. The experiments show the true signal strength is a slightly stronger than the simulations study in Chapter 2 would suggest.

In both the simulations and experimental results, the main reason for performance

deterioration beyond a certain $\alpha$ was the deterioration in signal strength. This may be combated in future iterations with an additional light source present. Simultaneously it is important to investigate what the true SNR would be in a surgical setting. There was very limited background noise present in these experiments due to the highly controlled environment. It is possible that DRS would still work even if the signal strength deteriorates more than 50% if the SNR remains strong enough. Should that be the case, DRS may perform well at even higher values of $\alpha$ and the detection depth may be greater.

The outcomes of this study provide valuable insights for the research being conducted into healthcare technologies, which need studies such as this one to bring forward different, innovative approaches of using optical sensing technology in medical applications. Specifically, the findings will be used to further advance the development of an optical sensing technique for the steerable bone drill currently being developed by researchers at the TU Delft [33]. Additionally, the results of this study make it clear that good performance of DRS at different protrusions is possible and can provide guidance to surgeons, particularly in LMICs (Low- or middle- income countries). Cutting edge sensing technologies can require highly complex hardware and may not be a feasible option for many hospitals. In contrast, DRS is based on fundamental principles and does not require highly complex materials or concepts to work, as shown in this study.

## 4.2. Future Recommendations

Collectively, the results of this work show that a bone awl using DRS as a guidance aid is possible. Such a bone awl has the potential to improve patient outcomes and reduce surgeon error. Achieving the ultimate goal of realizing a commercially viable bone awl that can provide real-time guidance to surgeons still requires many intermediate steps be taken first. This study provides a proof of concept for the technology in this context and does not consider at which values of $\alpha$ the bone awl becomes too blunt, potentially discouraging surgeons from using it. Beyond the context of a bone awl, this technology has the potential to be applied to other needle-shaped medical devices.

The immediate next step is to consider how DRS performance is affected when the optical fiber arrangement is changed, but within the context of a needle shape. Specifically two new fiber arrangements should be considered.

1. The performance of DRS when a second light source is placed opposite of the LE fiber relative to the LC fiber. This is visualized in Figure 4.1a. In theory the DRS performance will increase when measured by the same parameters as in this study, because the signal strength will increase due to the second light source. The performance of DRS when a second light source is placed opposite of the LE fiber relative to the LC fiber. This is visualized in Figure 4.1a. In theory the DRS performance will increase when measured by the same parameters as in this study, because the signal strength will increase due to the second light source.
2. The second fiber arrangement places the LC fiber and LE fiber on opposite sides of the needle's tip with the same distance to the tip between them. This means the performance of the DRS will not be impacted by a protrusion, however the

tip of the needle may affect the signal as it could interact with light. This is also shown in figure 4.1b. Beyond these ideas, other constellations with potentially more optical fibers may be considered. All arrangements must consider how many fibers to use, as using too many can compromise the rigidness of the entire structure. This is due to a significant percentage of the bone awl's volume must be hollowed out to allow for the placement of the fibers.

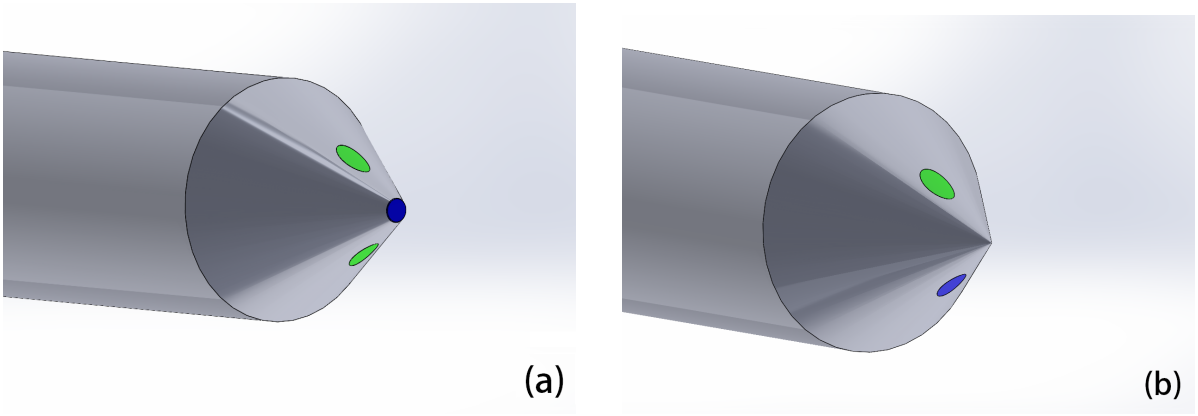


**(a)** In addition to the first LE and LC fibers, a second LE fiber is placed opposite of the first LE fiber.

**(b)** The LE and LC fibers are placed at the same height which the needle tip between them.

**Figure 4.1:** Visualization of a potential future optical fiber arrangement on the tip of a bone awl. The LE fibers are in green and the LC fibers are in blue.

After the optimal fiber constellation has been identified, further material studies are necessary to identify the best one for the final bone awl. Mechanical testing is required to ensure the material has strong enough mechanical properties to penetrate cancellous bone. The material must also be bio-compatible to ensure no adverse reactions from patients. Particular attention needs to be given to the glue chosen to fixate the optical fibers. It too must be strong enough to keep the fibers in place during surgeries and must not react with any commercially used cleaning and disinfecting products.

In addition to all the testing, the device will have to go through a certification process before it can enter the market. For approval in the European Union the device needs be classified as a class I medical device as it is an active, invasive device intended for transient use [35]. The device is considered active, as is requires a source of energy other than that generated by the human body for the DRS to operate. The bone awl is invasive and for transient use, as it will enter the body, but not spend more than 60 minutes inside. Following this, the final product could enter the EU market and by extension many secondary markets which also accept products which meet the EU standards for medical devices. Markets in the middle east and Africa approve the use of medical devices which meet the regulatory standards of the EU [28]. EU certification would therefore make the bone awl accessible to the target surgeons in LMICs.

## 4.3. Overall Conclusion

To summarize, the primary goal of the study was to understand how DRS would perform as a guidance aid to surgeons when integrated into a bone awl. This question was approached using Monte Carlo Simulations in MATLAB to determine until which needle sharpness, the signal strength and detection depth remain satisfactory. In

the simulations this was the case for all $\alpha \leq 30°$. The results were then validated experimentally, where a custom-designed optical probe was used in combination with coconut milk to simulate the optical properties of cancellous bone tissue. The experiments yielded good DRS performance for all $\alpha \leq 40^o$. The main reason for the different outcome of the simulations and experiments is that the simulations underestimated the true signal strength.

The key limitation of this study is that it does not consider how the performance of the bone awl itself is affected by needle sharpness. Factors such as which vertebrae is affected, patient age and personal preference may result in a bone awl being selected for use in a surgery that does not have the ideal sharpness for providing guidance using DRS. This must be taken into account when considering how the findings of this study can contribute to the greater goal of improved patient outcomes for patients *e.g.* a blunt device may have a more effective guidance, but fail in other performance criteria specific to a bone awl. The work presented considered whether DRS can be a viable optical sensing technology on needle shaped medical devices. In the presented context of a bone awl used for pedicle screw placement, DRS was successfully able to do so.

# References


[1] URL: https://www.go-tan.com/en/products/cocos/go-tan-kokosmelk-250-mlt-pak/.

[2] URL: https://www.thorlabs.com/navigation.cfm?guide_id=143.

[3] Safwan Alomari et al. "Safety and Accuracy of Freehand Pedicle Screw Placement and the Role of Intraoperative O-Arm: A Single-Institution Experience". In: *Spine* 48 (3 Feb. 2023), pp. 180–188. ISSN: 15281159. DOI: 10.1097/BRS.0000000000004497.

[4] Dangol Bijendra et al. "Adjacent Level Vertebral Fractures in Patients Operated with Percutaneous Vertebroplasty". In: *Open Journal of Orthopedics* 08 (03 2018), pp. 116–126. ISSN: 2164-3008. DOI: 10.4236/ojo.2018.83014.

[5] Jonathan P. Blitz. *Modern techniques in applied molecular spectroscopy*. Wiley, 1998, p. 410. ISBN: 0471123595.

[6] Gustav Burström et al. "Diffuse reflectance spectroscopy accurately identifies the pre-cortical zone to avoid impending pedicle screw breach in spinal fixation surgery". In: *Biomedical Optics Express* 10 (11 Nov. 2019), p. 5905. ISSN: 2156-7085. DOI: 10.1364/boe.10.005905.

[7] Dassault Systèmes SOLIDWORKS Corp. *2022*. Waltham, Massachusetts, United States, 2022. URL: https://www.solidworks.com/.

[8] Joana da Costa Reis and Maria Teresa Oliveira. "Bone: Functions, Structure and Physiology". In: *The Computational Mechanics of Bone Tissue: Biological Behaviour, Remodelling Algorithms and Numerical Applications*. Ed. by Jorge Belinha, Maria-Cristina Manzanares-Céspedes, and António M. G. Completo. Cham: Springer International Publishing, 2020, pp. 3–43. ISBN: 978-3-030-37541-6. DOI: 10.1007/978-3-030-37541-61. URL: https://doi.org/10.1007/978-3-030-37541-6_1.

[9] Sanford H. Davne and Donald L. Myers. "Complications of Lumbar Spinal Fusion with Transpedicular Instrumentation". In: *Spine* 17 (6 June 1992), S184–S189.

[10] Richard A Deyo et al. "United States Trends in Lumbar Fusion Surgery for Degenerative Conditions". In: *SPINE* 30 (12 2005), pp. 1441–1445. URL: www.ahrq.gov/HCUPnet..

[11] Gage Greening et al. "Sampling depth of a diffuse reflectance spectroscopy probe for in-vivo physiological quantification of murine subcutaneous tumor allografts". In: *Journal of Biomedical Optics* 23 (08 Aug. 2018), p. 1. ISSN: 15602281. DOI: 10.1117/1.jbo.23.8.085006.

[12] L G Henyey and J L Greenstein. "Diffuse radiation in the Galaxy". In: *Astrophysical Journal* 93 (1941), pp. 70–83.

[13] Tonya Hines. *Anatomy of the Spine*. Sept. 2018. URL: https://mayfieldclinic.com/pe-anatspine.htm (visited on 06/05/2023).

[14] The MathWorks Inc. *Optimization Toolbox version: 9.4 (R2022b)*. Natick, Massachusetts, United States, 2022. URL: https://www.mathworks.com.

[15] Jay Jagannathan. *Pedicle screws for spine fusion*. Oct. 2022. URL: https://www.spine-health.com/treatment/spinal-fusion/pedicle-screws-spine-fusion.

[16] Kazuyoshi Kobayashi et al. "Epidemiological trends in spine surgery over 10 years in a multicenter database". In: *European Spine Journal* 27 (8 Aug. 2018), pp. 1698–1703. ISSN: 14320932. DOI: 10.1007/s00586-018-5513-4.

[17] Victor Kosmopoulos and Constantin Schizas. "Pedicle Screw Placement Accuracy A Meta-analysis". In: *Spine Journal* 32 (3 2007), pp. 111–120. URL: http://journals.lww.com/spinejournal.

[18] Lucas Kreiß et al. "Diffuse reflectance spectroscopy and Raman spectroscopy for label-free molecular characterization and automated detection of human cartilage and subchondral bone". In: *Sensors and Actuators, B: Chemical* 301 (Dec. 2019). ISSN: 09254005. DOI: 10.1016/j.snb.2019.127121.

[19] Maria Lepore and Ines Delfino. "Intralipid-Based Phantoms for the Development of New Optical Diagnostic Techniques". In: *The Open Biotechnology Journal* 13 (1 Dec. 2019), pp. 163–172. ISSN: 1874-0707. DOI: 10.2174/18740707019013016 3.

[20] Yangyang Liu et al. "Monitoring the reduced scattering coefficient of bone tissues on the trajectory of pedicle screw placement using near-infrared spectroscopy". In: *Journal of Biomedical Optics* 19 (11 Nov. 2014), p. 117002. ISSN: 1083-3668. DOI: 10.1117/1.jbo.19.11.117002.

[21] Merle Losch et al. "Diffuse reflectance spectroscopy of the spine:improved breach detection with angulated fibers". In: *Biomedical Optics Express* 14 (Jan. 2023). DOI: 10.1364/BOE.471725.

[22] Dominik Marti et al. "MCmatlab: an open-source, user-friendly, MATLAB-integrated three-dimensional Monte Carlo light transport solver with heat diffusion and tissue damage". In: *Journal of Biomedical Optics* 23 (12 Dec. 2018), p. 1. ISSN: 15602281. DOI: 10.1117/1.jbo.23.12.121622.

[23] Alexander Mason et al. "The accuracy of pedicle screw placement using intraoperative image guidance systems: A systematic review". In: *Journal of Neurosurgery: Spine* 20 (2 Feb. 2014), pp. 196–203. ISSN: 15475654. DOI: 10.3171/2013.11.SPINE13413.

[24] Kamran Mohiuddin and Scott J. Swanson. "Maximizing the benefit of minimally invasive surgery". In: *Journal of Surgical Oncology* 108 (5 Oct. 2013), pp. 315–319. ISSN: 00224790. DOI: 10.1002/jso.23398.

[25] Emilie Pery et al. "Spectral features selection and classification for bimodal optical spectroscopy applied to bladder cancer in vivo diagnosis". In: *IEEE Transactions on Biomedical Engineering* 61 (1 Jan. 2014), pp. 207–216. ISSN: 00189294. DOI: 10.1109/TBME.2010.2103559.

[26] S A Prahl et al. "A Monte Carlo Model of Light Propagation in Tissue". In: *Dosimetry of Laser Radiation in Medicine and Biology* 5 (1989), pp. 102–111.

[27] Ahmad Jabir Rahyussalim et al. "Osteoporotic pedicle screw: Review of various types of pedicle screw and cement augmentation". In: vol. 2193. American Institute of Physics Inc., Dec. 2019. ISBN: 9780735419445. DOI: 10.1063/1.5139323.

[28] *Regulatory Affairs: Approval Medical Devices: Middle East and Africa 2021*. June 2021. URL: https://www.qtec-group.com/en/approval-medical-devices-the-middle-east-and-africa/.

[29] B. G. Santoni et al. "Cortical bone trajectory for lumbar pedicle screws". In: *Spine Journal* 9 (5 May 2009), pp. 366–373. ISSN: 15299430. DOI: 10.1016/j.spinee.2008.07.008.

[30] Afshan Shirkavand et al. "Non-invasive Reflectance Spectroscopy for Normal and Cancerous Skin Cells Refractive Index Determination: An In Vitro Study". In: *Lasers in Surgery and Medicine* 51 (8 Oct. 2019), pp. 742–750. ISSN: 10969101. DOI: 10.1002/lsm.23095.

[31] Florian Stelzle et al. "Optical Nerve Detection by Diffuse Reflectance Spectroscopy for Feedback Controlled Oral and Maxillofacial Laser Surgery". In: *Journal of Translational Medicine* 9 (Feb. 2011). ISSN: 14795876. DOI: 10.1186/1479-5876-9-20.

[32] Akash Swamy et al. "Diffuse reflectance spectroscopy for breach detection during pedicle screw placement: A first in vivo investigation in a porcine model". In: *BioMedical Engineering Online* 19 (1 June 2020). ISSN: 1475925X. DOI: 10.1186/s12938-020-00791-2.

[33] Akash Swamy et al. "Diffuse reflectance spectroscopy, a potential optical sensing technology for the detection of cortical breaches during spinal screw placement". In: *Journal of Biomedical Optics* 24 (01 Jan. 2019), p. 1. ISSN: 15602281. DOI: 10.1117/1.jbo.24.1.017002.

[34] Sandip P. Tarpada, Matthew T. Morris, and Denver A. Burton. "Spinal fusion surgery: A historical perspective". In: *Journal of Orthopaedics* 14 (1 Mar. 2017), pp. 134–136. ISSN: 0972978X. DOI: 10.1016/j.jor.2016.10.029.

[35] The European Parliament and the Council of the European Union. *Council regulation (EU) 2017/745*. https://eur-lex.europa.eu/legal-content/EN/TXT/PDF/?uri=CELEX:32017R0745. Apr. 2017.

[36] Caroline P. Thirukumaran et al. "National trends in the surgical management of adult lumbar isthmic spondylolisthesis: 1998 to 2011". In: *Spine* 41 (6 Mar. 2016), pp. 490–501. ISSN: 15281159. DOI: 10.1097/BRS.0000000000001238.

[37] Lihong Wang, Steven L Jacques, and Liqiong Zheng. *MCML-Monte Carlo modeling of light transport in multi-layered tissues*. 1995, pp. 131–146.

# A

# Solidworks Drawings

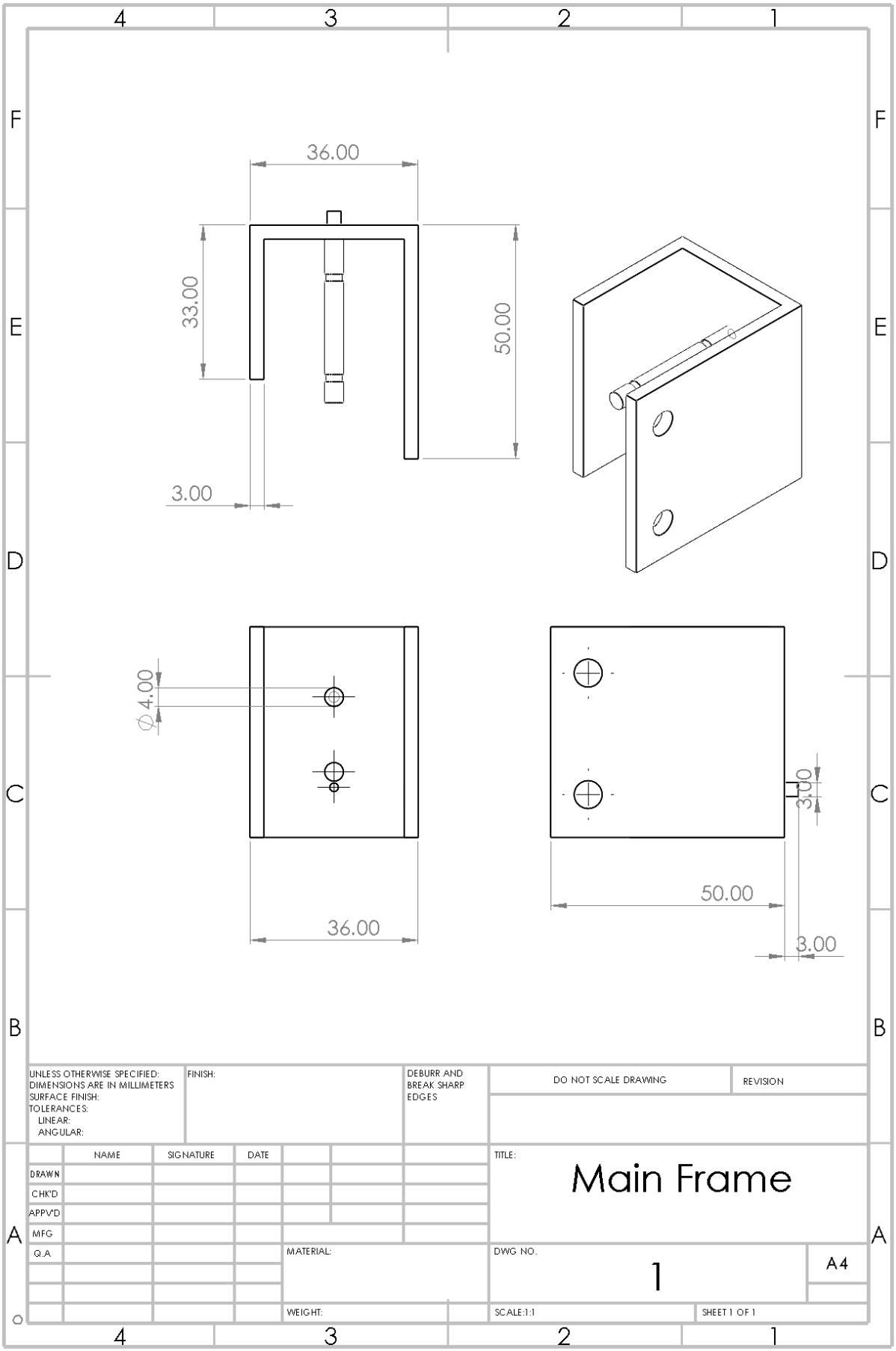


| | | | | | | |
|---|---|---|---|---|---|---|
| UNLESS OTHERWISE SPECIFIED:<br>DIMENSIONS ARE IN MILLIMETERS<br>SURFACE FINISH:<br>TOLERANCES:<br>LINEAR:<br>ANGULAR: | FINISH: | | DEBURR AND BREAK SHARP EDGES | DO NOT SCALE DRAWING | REVISION | |
| | NAME | SIGNATURE | DATE | TITLE: | | |
| DRAWN | | | | Main Frame | | |
| CHK'D | | | | | | |
| APPV'D | | | | | | |
| MFG | | | | | | |
| Q.A | | | | MATERIAL: | DWG NO. | A4 |
| | | | | | 1 | |
| | | | | WEIGHT: | SCALE:1:1 | SHEET 1 OF 1 |

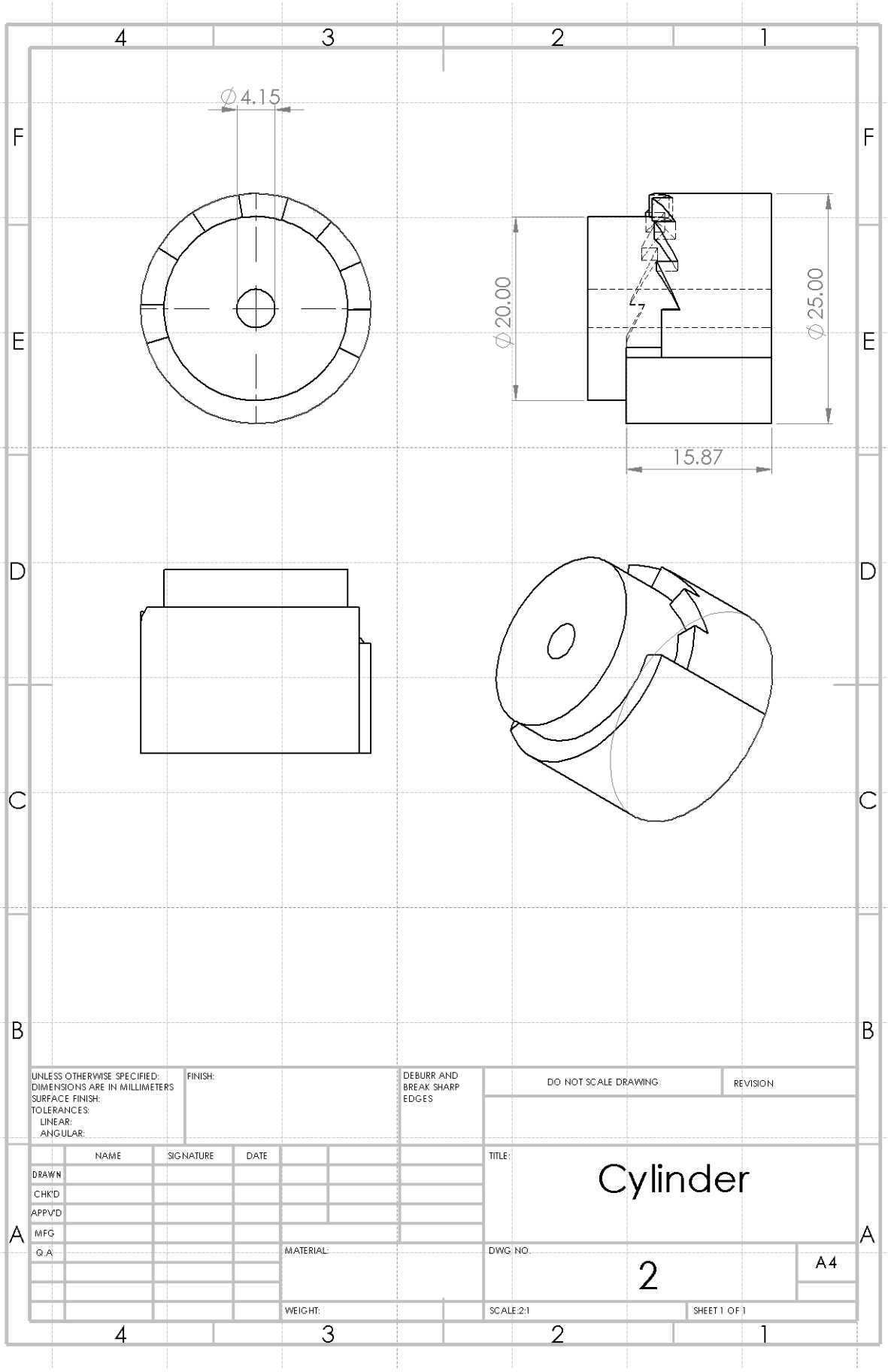
4
3
2
1
F
E
D
C
B
A
∅4.15
∅20.00
∅25.00
15.87
UNLESS OTHERWISE SPECIFIED:
DIMENSIONS ARE IN MILLIMETERS
SURFACE FINISH:
TOLERANCES:
LINEAR:
ANGULAR:
FINISH:
DEBURR AND BREAK SHARP EDGES
DO NOT SCALE DRAWING
REVISION
NAME
SIGNATURE
DATE
DRAWN
CHK'D
APPV'D
MFG
Q.A
MATERIAL:
WEIGHT:
TITLE:
Cylinder
DWG. NO.
2
A4
SCALE:2:1
SHEET 1 OF 1

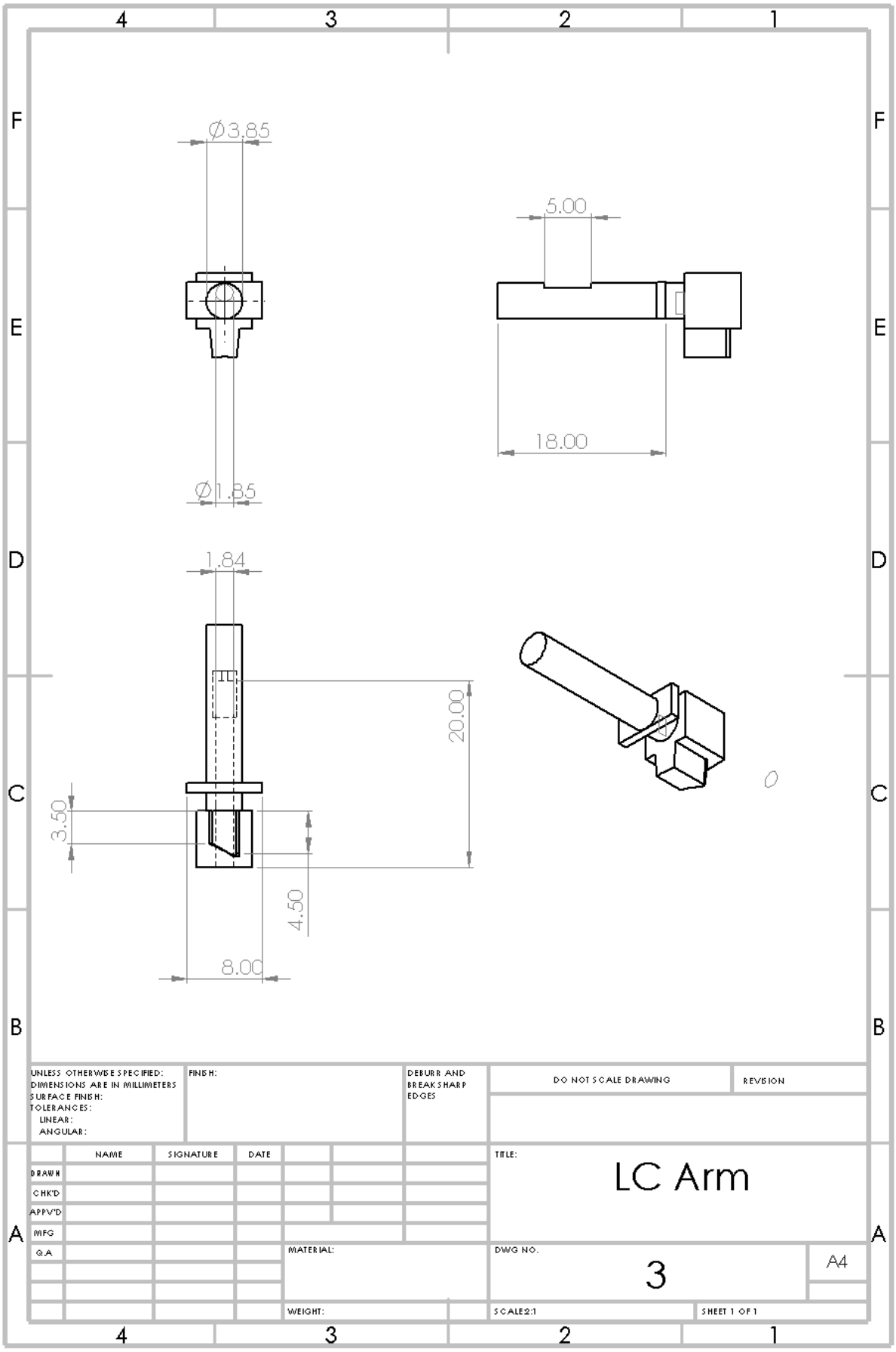
4
3
2
1
F
E
D
C
B
A
Ø3.85
Ø1.85
5.00
18.00
1.84
20.00
3.50
4.50
8.00
UNLESS OTHERWISE SPECIFIED:
DIMENSIONS ARE IN MILLIMETERS
SURFACE FINISH:
TOLERANCES:
LINEAR:
ANGULAR:
FINISH:
DEBURR AND BREAK SHARP EDGES
DO NOT SCALE DRAWING
REVISION
NAME
SIGNATURE
DATE
DRAWN
CHK'D
APP'V'D
MFG
Q.A
TITLE:
LC Arm
MATERIAL:
DWG NO.
3
A4
WEIGHT:
SCALE:2:1
SHEET 1 OF 1

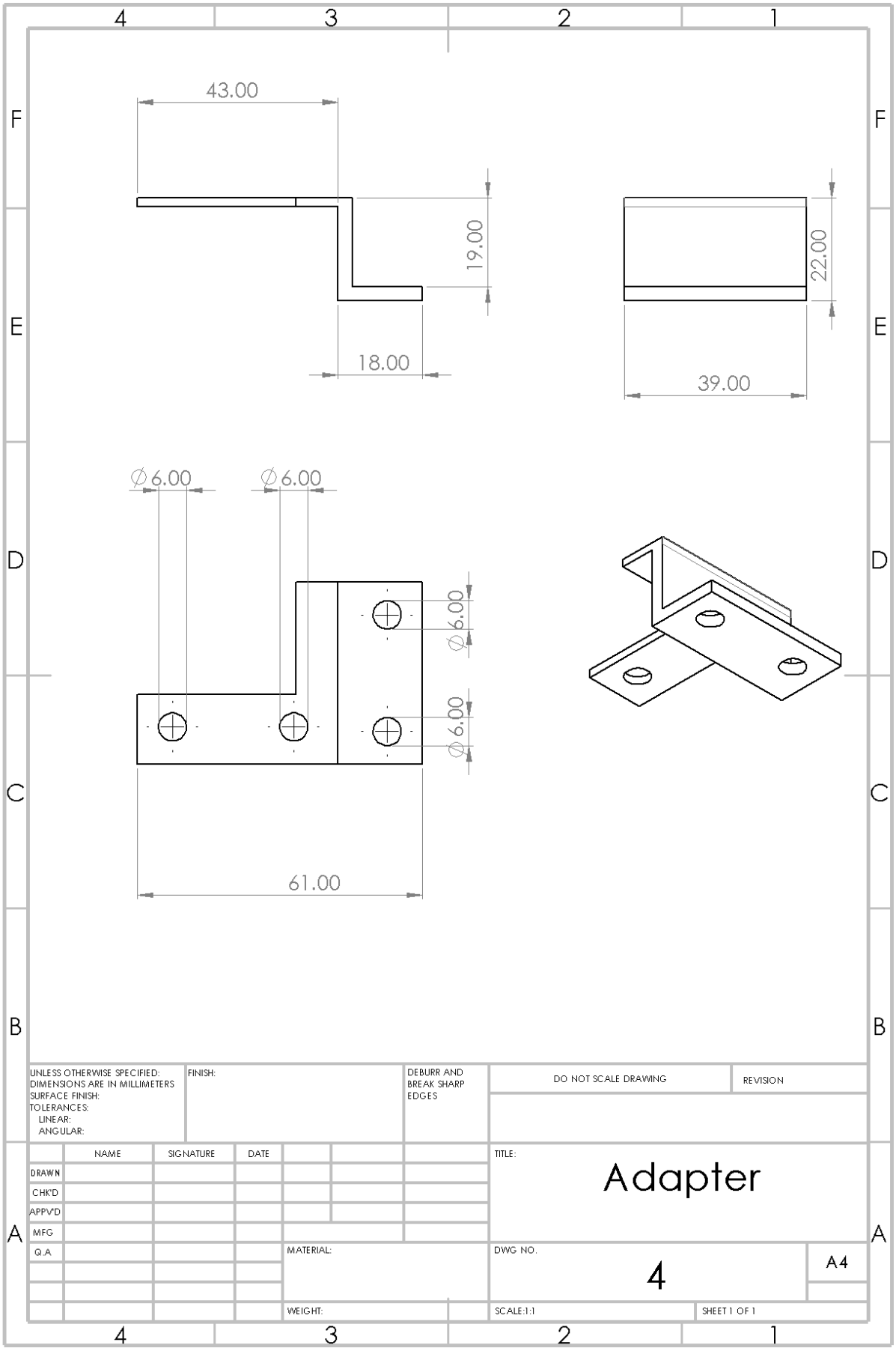


| | | | | | | |
|---|---|---|---|---|---|---|
| UNLESS OTHERWISE SPECIFIED:<br>DIMENSIONS ARE IN MILLIMETERS<br>SURFACE FINISH:<br>TOLERANCES:<br>LINEAR:<br>ANGULAR: | FINISH: | | DEBURR AND BREAK SHARP EDGES | | DO NOT SCALE DRAWING | REVISION |
| | NAME | SIGNATURE | DATE | | TITLE: | |
| DRAWN | | | | | Adapter | |
| CHK'D | | | | | | |
| APPV'D | | | | | | |
| MFG | | | | | | |
| Q.A | | | | MATERIAL: | DWG NO. | A4 |
| | | | | | 4 | |
| | | | | WEIGHT: | SCALE:1:1 | SHEET 1 OF 1 |

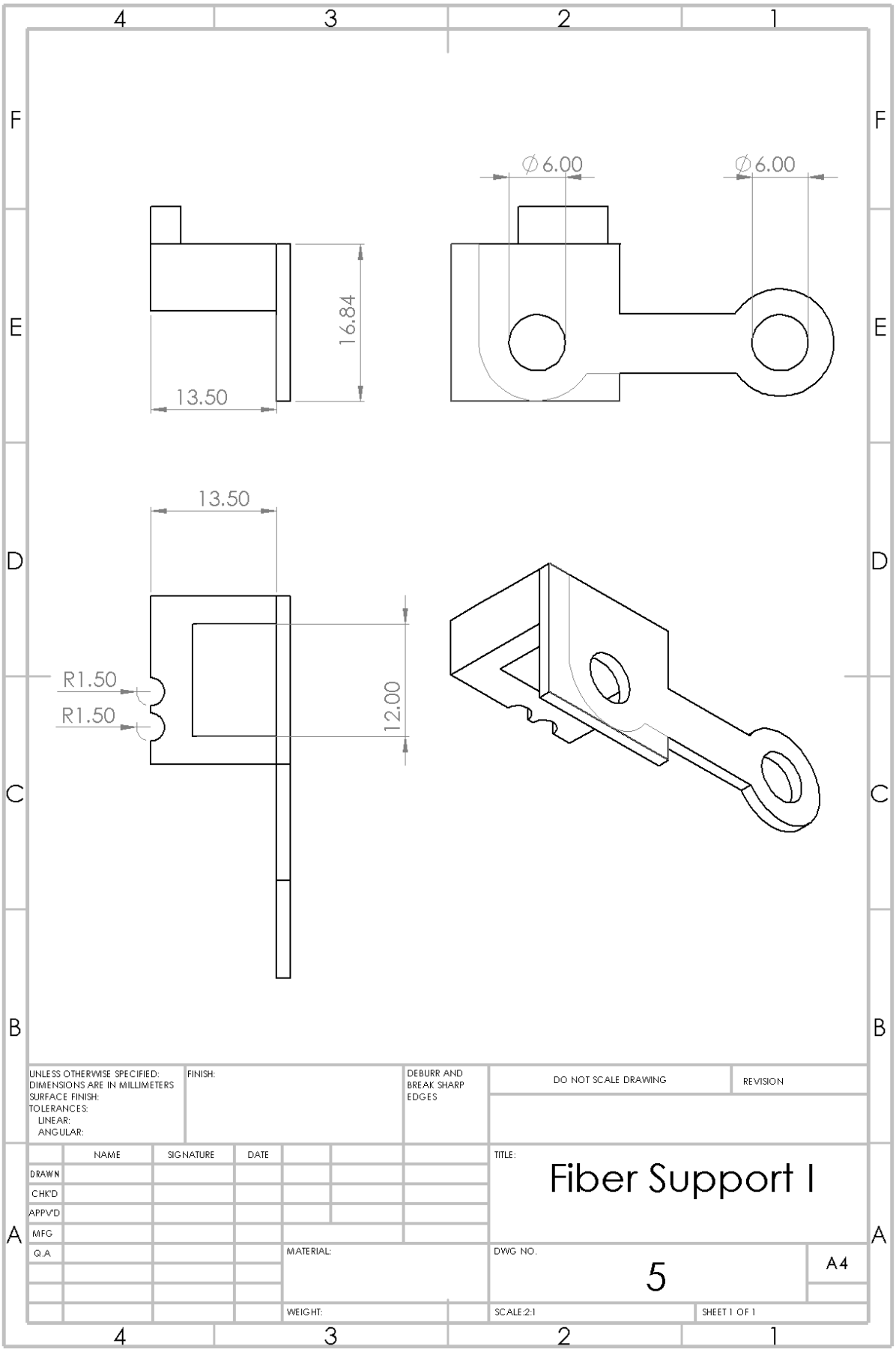
4
3
2
1
F
E
D
C
B
A
∅6.00
∅6.00
16.84
13.50
13.50
R1.50
R1.50
12.00
UNLESS OTHERWISE SPECIFIED:
DIMENSIONS ARE IN MILLIMETERS
SURFACE FINISH:
TOLERANCES:
LINEAR:
ANGULAR:
FINISH:
DEBURR AND BREAK SHARP EDGES
DO NOT SCALE DRAWING
REVISION
NAME
SIGNATURE
DATE
DRAWN
CHK'D
APPV'D
MFG
Q.A
TITLE:
Fiber Support I
MATERIAL:
DWG NO.
5
A4
WEIGHT:
SCALE:2:1
SHEET 1 OF 1

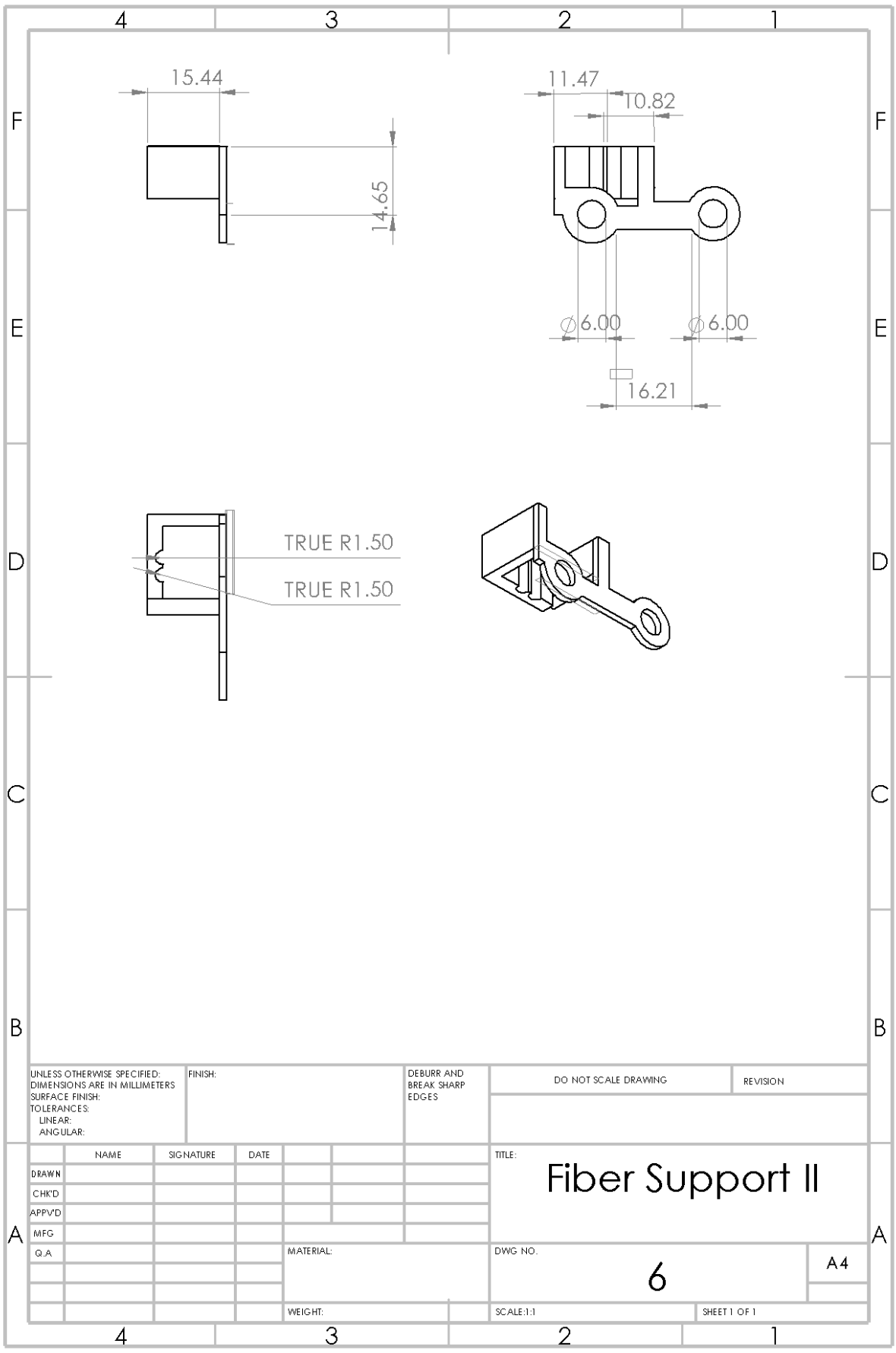


| | | | |
|---|---|---|---|
| UNLESS OTHERWISE SPECIFIED:<br>DIMENSIONS ARE IN MILLIMETERS<br>SURFACE FINISH:<br>TOLERANCES:<br>LINEAR:<br>ANGULAR: | FINISH: | DEBURR AND BREAK SHARP EDGES | DO NOT SCALE DRAWING / REVISION |

| | NAME | SIGNATURE | DATE |
|---|---|---|---|
| DRAWN | | | |
| CHK'D | | | |
| APPV'D | | | |
| MFG | | | |
| Q.A | | | |

TITLE: Fiber Support II

MATERIAL:

DWG NO. 6

A4

WEIGHT:

SCALE:1:1

SHEET 1 OF 1